



VIROLOGY

Intercellular communication within the virus microenvironment affects the susceptibility of cells to secondary viral infections

Bokai Song[†], Xinlei Sheng[†], Joshua L. Justice, Krystal K. Lum, Peter J. Metzger, Katelyn C. Cook, James C. Kostas, Ileana M. Cristea*

Communication between infected cells and cells in the surrounding tissue is a determinant of viral spread. However, it remains unclear how cells in close or distant proximity to an infected cell respond to primary or secondary infections. We establish a cell-based system to characterize a virus microenvironment, distinguishing infected, neighboring, and distal cells. Cell sorting, microscopy, proteomics, and cell cycle assays allow resolving cellular features and functional consequences of proximity to infection. We show that human cytomegalovirus (HCMV) infection primes neighboring cells for both subsequent HCMV infections and secondary infections with herpes simplex virus 1 and influenza A. Neighboring cells exhibit mitotic arrest, dampened innate immunity, and altered extracellular matrix. Conversely, distal cells are poised to slow viral spread due to enhanced antiviral responses. These findings demonstrate how infection reshapes the microenvironment through intercellular signaling to facilitate spread and how spatial proximity to an infection guides cell fate.

INTRODUCTION

Cell-to-cell communication is the basis of multicellular life, response to environmental cues, and development of disease. The remarkable capacity of viruses to manipulate host intracellular processes is essential for establishing an infection, but less is understood about how viruses control intercellular communication and how this affects the spread of infection in tissue. Primary infection of a cell or reactivation from viral latency establishes a localized virus microenvironment (VME). In a VME, cell nonautonomous signaling pathways must be reprogrammed by either the virus or the host to promote or suppress viral spread, respectively. From the perspective of the host, intracellular sensing of pathogen-associated molecular patterns derived from the virus leads to activation of intrinsic and innate immune responses to induce the secretion of type I interferons (IFNs), other cytokines, and chemokines [reviewed in (1)]. Receptor-mediated recognition of these signaling molecules by uninfected cells adjacent to the infection site induces the expression of IFN-stimulated genes (ISGs), which restrict intrinsic viral entry and replication (2). Innate and adaptive immune cells, including natural killer cells, B cells, and T cells, are further recruited to clear the infection *in vivo* (3). However, in a VME, infection-adjacent cells that receive transduced messages may concomitantly undergo proviral alterations to promote virus spread.

Mechanisms by which viruses influence uninfected cells in their local environment are now coming to light. In many cases, viruses influence the VME in a manner that is unique to the pathobiology of that virus. For example, measles virus infection of the human airway causes localized proliferation of uninfected cells beneath the infectious center, which may be a mechanism to dislodge the infected cells for viral population spread (4). However, when

comparing viruses from different families, there may be convergent proviral VME phenotypes. For example, both hepatitis B virus and enteroviruses can dampen immune responses in uninfected cells by delivering anti-inflammatory microRNA via extracellular vesicles (EVs) that shed from the infected cell (5, 6). Herpes virus-induced EVs have been shown to contain proteins of both viral and host origin, viral mRNA, and viral miRNA (7–10). EVs purified from human cytomegalovirus (HCMV)-infected cells promote virus spread in a manner both dependent and independent of endosomal sorting (9). Together, it is now evident that viruses have acquired strategies to influence the microenvironment, which must be deciphered to understand viral pathogenesis.

Conventionally, the impacts of virus infection on host cells have been investigated by comparing infected to mock-infected cells collected from separate cultures or tissues. Alternatively, infected cells have been compared to the aggregate sum of those remaining from a population using enrichment methods (e.g., tagged virus strains and enrichment via the tag). However, these approaches do not distinguish more than the two populations of infected and uninfected cells from the same sample. Single-cell sequencing of tissue and cells also offers a glimpse into the interactions in heterogeneously infected populations of cells (11, 12). In addition, a study developed an antibody-based protein and nucleic acid imaging method to simultaneously assess more than 30 cell markers *in situ* in tissues infected with simian immunodeficiency virus (13). However, these approaches would be enhanced by an ability to both discriminate and isolate nearby and distant cellular subpopulations. Such subpopulations may have distinct response programs based on how cells send messages through transcellular interactions and soluble mediators. An approach that would provide both spatial discrimination and isolation would facilitate a more complete spatial understanding and characterization of VME dynamics. There are also limited studies that define the functional consequences of spatial proximity to an infection. Given these paucities, it remains largely unknown not only how uninfected cells in close (neighboring) or

Copyright © 2023 The Authors, some rights reserved; exclusive licensee American Association for the Advancement of Science. No claim to original U.S. Government Works. Distributed under a Creative Commons Attribution NonCommercial License 4.0 (CC BY-NC).

Downloaded from <https://www.science.org> at University of Wisconsin Madison on October 31, 2024

Department of Molecular Biology, Princeton University, Washington Road, Princeton, NJ 08544, USA.

[†]These authors contributed equally to this work.

*Corresponding author. Email: icristea@princeton.edu

distant (distal) proximity to an infected cell respond to a primary infection but also how cell spatial address in a VME influences susceptibility to secondary infections.

Here, we adapted a secreted, cell-permeable fluorescent protein labeling approach paired with cell sorting (14) to spatially discriminate and enrich for HCMV infected, neighboring, and distal cell subpopulations within a VME. HCMV is a herpesvirus that has co-evolved with human hosts for more than 100 million years. Primary infection by HCMV occurs in fibroblast and epithelial cells of the skin or mucosa. Thereafter, the virus spreads and establishes life-long latent infection in myeloid lineage cells that is characterized by periodic reactivation events (15). HCMV is the leading cause of congenital birth defects and, in immunosuppressed adults, is linked to direct end-organ diseases and indirect posttransplantation effect (16). In addition, as an oncomodulatory virus, HCMV triggers pro-oncogenic pathways and favors cancer malignancy (17). Cell-to-cell communication is a central determinant of HCMV primary infection, latency, and reactivation as well as of the host immune response to inhibit viral spread. Within infected individuals, HCMV infection is linked to marked reorganization of nearly every aspect of the cellular landscape, including organelle spatial and contact site remodeling (18, 19), metabolic reprogramming (20), and cell cycle manipulation to promote viral replication in G₁ phase (21). Simultaneously, the virus has adapted to effectively suppress DNA sensing and immune signaling. These viral strategies are aimed toward promoting virus replication and spread (22, 23). Moreover, the extensive reorganization of host cell organelles and membranes that occurs during infection affects intercellular communication (9, 18), including secretory pathways that release membrane-enclosed EVs. Blocking EVs during HCMV infection slows the spread of the virus in tissue culture, suggesting that HCMV uses EVs to prime subsequent rounds of viral infection (9). Thus, HCMV infection represents a meaningful system to study cell-cell communication within a VME.

By adapting a system to distinguish and isolate cells based upon proximity to HCMV infection, we sought to resolve proteome signatures of the heterogeneous response to infection that drive susceptibility or resistance to subsequent rounds of viral infection. We integrated fluorescence-activated cell sorting (FACS), quantitative mass spectrometry (MS), confocal microscopy, and cell cycle assays to establish molecular features and infection outcomes of cells within an HCMV microenvironment. In neighboring compared to distal cells, we find proviral signatures, including lower levels of IFN-inducible and extracellular matrix (ECM) proteins. We demonstrate that neighboring cells exhibit increased susceptibility to secondary infections with either HCMV or other nuclear-replicating viruses [herpes simplex virus 1 (HSV-1) and influenza A]. Unexpectedly, we found that the cells most proximal to HCMV infection undergo accelerated cell cycle entry with prolonged mitotic arrest—a finding with implications in HCMV spread and HCMV-linked oncogenesis. Distal and mock-infected cells exhibited distinct proteome profiles, providing evidence for how a primary infection influences cell features across multiple levels of spatial proximity. Together, our study demonstrates that cellular spatial address in a VME guides cell fates by engendering susceptibility to secondary infections, with signatures in proteome composition and cell cycle progression. Our findings form the foundation for how virus infection reshapes the surrounding

environment, highlighting the temporal and spatial complexities of inter- and intracellular communication within a VME.

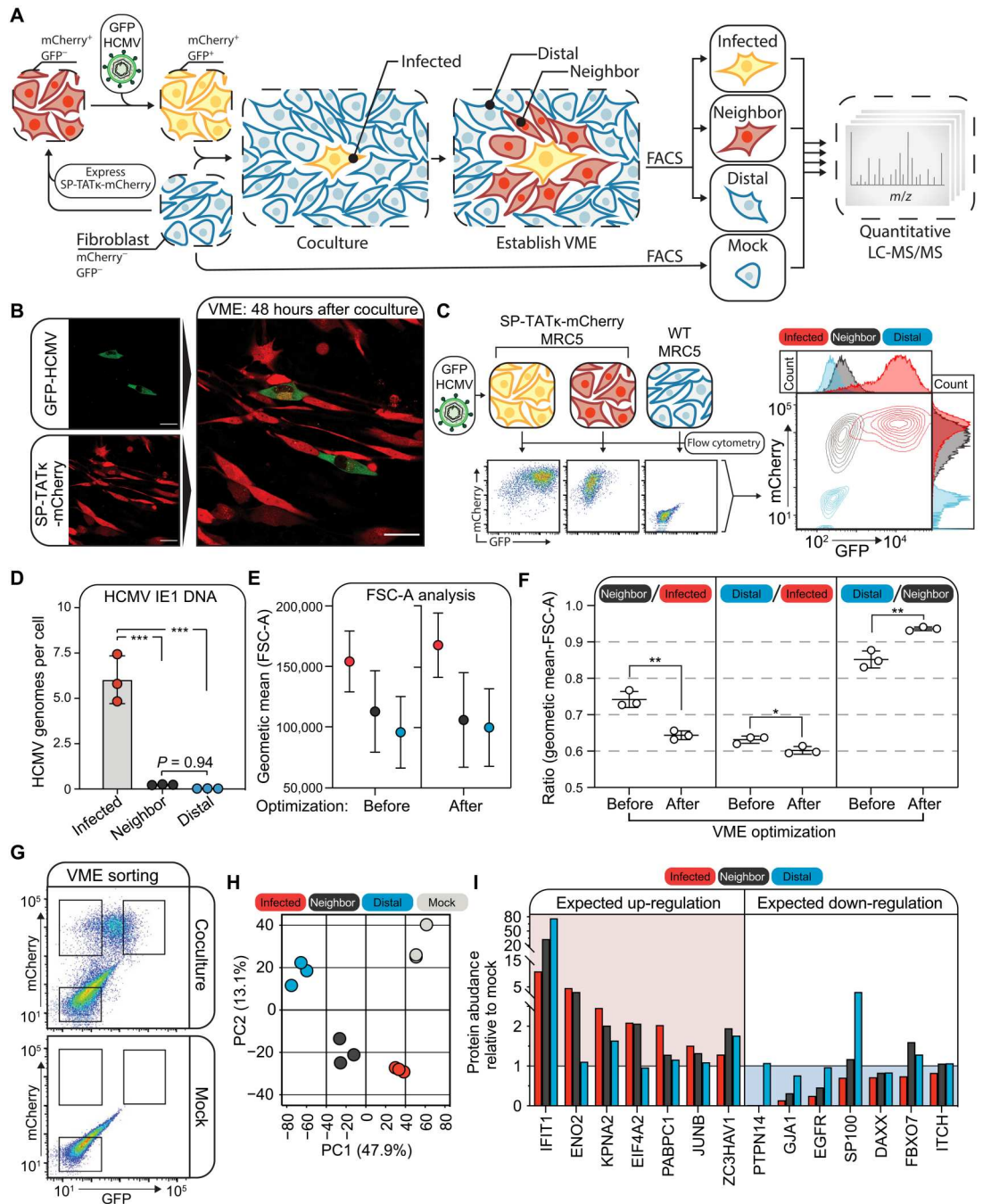
RESULTS

Establishing a workflow for characterizing the VME

To design an experimental workflow that distinguishes infected, neighboring, and distal cell populations, we adapted the lipid-permeable fluorescent protein labeling strategy previously reported for studying the tumor microenvironment (14). Specifically, we constructed a protein that contains mCherry fused to a secretory signal peptide (SP) and a lipid-permeable peptide, TAT κ , modified from the HIV-1 trans-acting activator of transcription (TAT). The resulting SP-TAT κ -mCherry protein was expressed in human fibroblasts (Fig. 1A) and was not found to affect the kinetics of HCMV infection (fig. S1A). To investigate the VME, the SP-TAT κ -mCherry cells were infected with an HCMV strain tagged with green fluorescent protein (GFP). We selected an UL32-GFP HCMV strain, in which pUL32 is a viral protein that directly interacts with the viral capsid and for which we have previously shown to exhibit similar growth kinetics to wild-type (WT) HCMV during its 4- to 5-day replication cycle. To ensure homogenous infection of all cells, the SP-TAT κ -mCherry cells were infected with UL32-GFP HCMV for 1 hour at a high multiplicity of infection [(MOI) of 5]. The infected cells were then cocultured with WT (uninfected) fibroblasts at an optimized ratio of 1:10 (fig. S1C). Given that SP leads to mCherry secretion and TAT κ mediates cell entry, the infected cells were allowed to label the neighboring cells in red for 24, 48, or 72 hours (fig. S1B). The 48-hour period provided a suitable ratio of labeled and unlabeled cells to enable the further separation of neighboring and distal cells (fig. S1B). By microscopy, the ability of infected SP-TAT κ -mCherry (GFP⁺/mCherry⁺) cells to label neighboring cells with mCherry (GFP⁻/mCherry⁺) was evident following 48 hours of coculturing (Fig. 1B).

Identification of suitable coculturing and labeling conditions allowed us next to separate the infected, neighboring, and distal cell populations by flow cytometry analysis (Fig. 1C). Using experimentally derived gating conditions that enriched for the three populations, more than 30,000 cells were sorted in each of the infected (GFP⁺/mCherry⁺), neighboring (GFP⁻/mCherry⁺), and distal (GFP⁻/mCherry⁻) cell populations (fig. S1, D and E). Although at 48 hours post infection (hpi), the HCMV replication cycle in the infected cells is not yet complete, and viral particles are not yet released, thereby enabling us to investigate the surrounding neighboring and distal cells still in an uninfected state. Thus, we aimed to verify that neighboring and distal cells are not infected by HCMV. We conducted quantitative polymerase chain reaction (qPCR) to quantify HCMV genomic DNA in the sorted populations. The qPCR results indicated significantly less viral DNA in neighboring and distal cells than in the infected cells, suggesting that our FACS parameters efficiently enriched for distinct VME subpopulations of cells (Fig. 1D). To further improve upon the ability to distinguish HCMV-infected and HCMV-uninfected cells within the VME, we used the knowledge that HCMV infection results in increased cell size and additionally analyzed the forward scatter profile (FSC-A) of the sorted VME populations (fig. S1, D and E). As expected, the mean FSC intensity of the sorted populations correlated with infection status (fig. S1F). Accordingly, we further refined the VME FACS parameters, increasing the gating

Fig. 1. Distinguish and enrich infected, neighboring, and distal cell populations. (A) Workflow for characterizing the human cytomegalovirus (HCMV) microenvironment. SP-TATκ-mCherry MRC5s were generated then infected with UL32-GFP (green fluorescent protein) HCMV. Coculturing of wild-type (WT) MRC5 with infected SP-TATκ-mCherry cells resulted in mCherry labeling of uninfected neighboring cells. All virus microenvironment (VME) cells were sorted by fluorescence-activated cell sorting (FACS) to enrich for infected (GFP⁺/mCherry⁺), neighboring (GFP⁻/mCherry⁺), and distal (GFP⁻/mCherry⁻) populations. Mock-infected WT cells were independently sorted. Sorted cells were subjected to mass spectrometry (MS) analysis. *m/z*, mass/charge ratio; LC-MS/MS, liquid chromatography coupled to tandem MS. (B) Representative immunofluorescence (IF) image of neighboring cell labeling upon 1:10 coculture with infected SP-TATκ-mCherry cells at 48 hours post infection (hpi). Scale bars, 100 μm. (C) Flow cytometry analysis of WT control, SP-TATκ-mCherry MRC5 cells infected by GFP-HCMV for 48 hours at a multiplicity of infection (MOI) of 5. Overlaid density plot lines indicate 10%. (D) Quantitative polymerase chain reaction (qPCR) of viral genomic DNA (IE1/UL123 sequence) per cell from sorted VME cocultures (*n* = 3 biological replicates). Error bar, SD. Significant differences were evaluated by analysis of variance (ANOVA) with Tukey correction ****P* < 0.001. (E) Mean forward scatter intensity (FSC-A) for each sorted VME cell population as a correlate for cell diameter. Shown is a representative FSC-A distribution for preoptimized and optimized FACS sorting conditions to better distinguish infected and uninfected cells. Bars: SD. (F) Calculated FSC-A ratios as in (E). Values closer to 1.00 indicate similarity of FSC-A profile. Bars: means ± SD. **P* < 0.05; ****P* < 0.01. (G) Representative (of *n* = 3) FACS plot of VME and mock cell populations used for proteomic investigation. (H) Principal components analysis (PCA) of infected, neighboring, distal, and mock cells. (I) Validation of expected protein abundance changes due to HCMV infection, with comparisons among infected, neighboring, and distal cells, relative to mock.



stringency, to separate more discrete populations of infected, neighboring, and distal cells (Fig. 1, E and F; and fig. S1, G and H). Using this combination of optimized parameters, we again sorted the cellular populations within the VME at 48 hours after coculture (1:10 ratio). In parallel, we independently sorted uninfected WT cells (GFP⁻/mCherry⁻) as a negative control (Fig. 1G and fig. S1I).

To decipher cellular proteome alterations within the VME, sorted cell populations (fig. S1I) were subjected to quantitative MS analyses, through which more than 5000 host proteins and 93 HCMV proteins were detected (tables S1 and S2). While the overall protein numbers and abundances were similar across all samples (fig. S2, A to D), principal components analysis (PCA) of the

Downloaded from https://www.science.org at University of Wisconsin Madison on October 31, 2024

proteomes indicated that the four cell populations are distinct (Fig. 1H). Further confirming that our workflow and infection conditions recapitulated known HCMV-induced protein alterations, we observed several expected changes in the abundance of host proteins (Fig. 1I and fig. S2E). Among the proteins with increased abundances in infected cells were antiviral proteins, such as interferon induced protein with tetratricopeptide repeats 1 (IFIT1) and zinc finger CCCH-type antiviral protein 1 (ZC3HAV1) (24, 25), which may contribute to early host defenses to the infection. Also increased were translational machinery components, including eukaryotic translation initiation factor 4A2 (EIF4A2), as well as the poly(A)-binding protein (PABP) and eIF4F initiation complex binding partner PABPC1. This observation is consistent with the reported HCMV-induced strategy to enhance eIF4F activity and translation initiation during productive replication (26). The nuclear import factor karyopherin subunit alpha-2 (KPNA2) and neuron-specific enolase ENO2 were also elevated, which were reported to be important for efficient viral genome synthesis (27) and tissue atypical metabolism through glycolysis and pyrimidine sugar production (28), respectively. Concurrently, we identified expected decreases in proteins including proteasome-degraded factors, such as the protein tyrosine phosphatase PTPN14, antiviral constituents of promyelocytic leukemia (PML) nuclear bodies, SP100, and death domain associated protein (DAXX) (25, 29), and the gap junction protein alpha 1 (GJA1) (25, 30). We also observed known decreases in E3 ubiquitin ligase components, including F-box only protein 7 (FBXO7) and E3 ubiquitin-protein ligase Itchy homolog (ITCH) (23, 31), as well as the well-recognized reduction in the receptor tyrosine kinase epidermal growth factor receptor (EGFR) for efficient HCMV entry and virion production (32). In summary, we adapted and designed a workflow to discriminate and enrich for infected, neighboring, and distal cell populations to map molecular features within a VME. Host cell markers of viral infection were detected in the infected cell population, and protein abundance profiles principally distinguished each cell population from one another.

A subset of viral proteins is detected in cells adjacent to the infection center

In analyzing the proteomes of the infected, neighboring, and distal cell populations, we first focused on monitoring viral proteins (Fig. 2, fig. S3, and table S1). As expected, we observed an overall abundance trend of infected > neighboring > distal for viral proteins, supporting that the enrichment of each cell population was efficient. The detected viral proteins were further categorized by their known arrangement within a virus particle (Fig. 2, A to D) and expression phase during the virus replication cycle (Fig. 2A and fig. S3, A and B). Specifically, we monitored the levels of viral capsid, envelope, tegument, and nonstructural proteins in each cell population. While capsid and envelope proteins were not represented in the neighboring or distal cells, a subset of tegument and nonstructural proteins were detected in the neighboring cells (Fig. 2, C and D). The minimal levels of capsid and envelope proteins, in conjunction with the presence of tegument proteins, suggest that these viral proteins in the neighboring cells may derive from secretion from infected cells rather than a lytic infection. This possibility was also supported when considering the temporality of viral protein expression. HCMV replication within an infected cell relies on a temporal cascade of viral gene expression, proceeding through immediate

early (IE), delayed early (DE), leaky late (LL), and true late (L) stages. We found that more IE and DE proteins, rather than L proteins, were detected in the neighboring cells (fig. S3, A and B), which is consistent with a transition from early to late stages of infection after 24 to 36 hpi. To further validate our observation, we quantified HCMV proteins using a targeted, parallel reaction monitoring (PRM) MS assay that we recently developed for targeted herpesvirus protein detection (i.e., TRUSTED assay) (33). We selected HCMV proteins known to be expressed at different stages of an infection (Fig. 2E and fig. S4A). In agreement with our data-dependent proteome analysis, while all targeted viral proteins were detected in the infected cells, only a subset was observed in neighboring cells. Most of the proteins detected were from the IE temporal class (e.g., pUL13 and pUL37). However, even within this class, some viral proteins were barely detectable (e.g., pUL122, also known as IE2). This observation matches the limited detection of capsid proteins (Fig. 2A), suggesting that the presence of these viral proteins in neighboring cells results from protein secretion rather than from the progression through an early stage of infection.

To directly test that the presence of viral proteins in the neighboring cells does not result from the initiation of a viral infection from virions released by the infected cells, we repeated our VME study with the addition of cidofovir (CDV) (Fig. 2F). CDV is an HCMV antiviral compound that halts viral DNA replication. As expected, in the infected cells, the CDV treatment did not substantially affect the levels of viral IE and DE proteins but substantially decreased the abundance of LL and L proteins (Fig. 2H and table S3). Despite this decrease in LL and L proteins in infected cells, the neighboring cells still showed similar IE protein levels in the presence or absence of CDV treatment (Fig. 2G). Furthermore, the decrease in L and LL proteins was even more pronounced in neighboring than infected cells upon CDV treatment (Fig. 2H). This corresponded to a sharp, CDV-dependent decrease in capsid, envelope glycoproteins, and tegument proteins in the neighboring cells that is more pronounced than in the infected population (fig. S3C). These observations suggest that the presence of viral proteins within the neighboring population of cells is due to transmission from the infected population rather than from a new or ongoing infection.

Reports have shown that viral proteins or related viral mRNA can be released extracellularly from infected cells, before the completion of a virus replication cycle. This is, at least in part, accomplished through exosomes, as it was shown upon HCMV and HSV-1 infections (7–10). Our observations of the presence of specific IE and DE proteins, and limited presence of capsid proteins, agree with such a communication between infected and neighboring cells before the release of virions. To assess whether EVs contribute to the presence of viral proteins in the neighboring population of cells, we treated HCMV-infected cells with the EV inhibitors, manumycin A and GW4869, which inhibit exosome secretion and biogenesis, respectively (Fig. 2I). Cell viability was not substantially affected by either manumycin A or GW4869 treatment (fig. S3H). At 48 hpi, we harvested supernatant from the infected cells and applied this to uninfected fibroblasts. Allowing 6 hours for EV uptake, we performed targeted MS for HCMV proteins (TRUSTED assay). Inhibition of either EV biogenesis or uptake significantly decreased the presence of all classes of viral proteins in the recipient fibroblasts (Fig. 2J and table S4). In addition, we assessed the assembly of EV-associated protein complexes, exocyst and

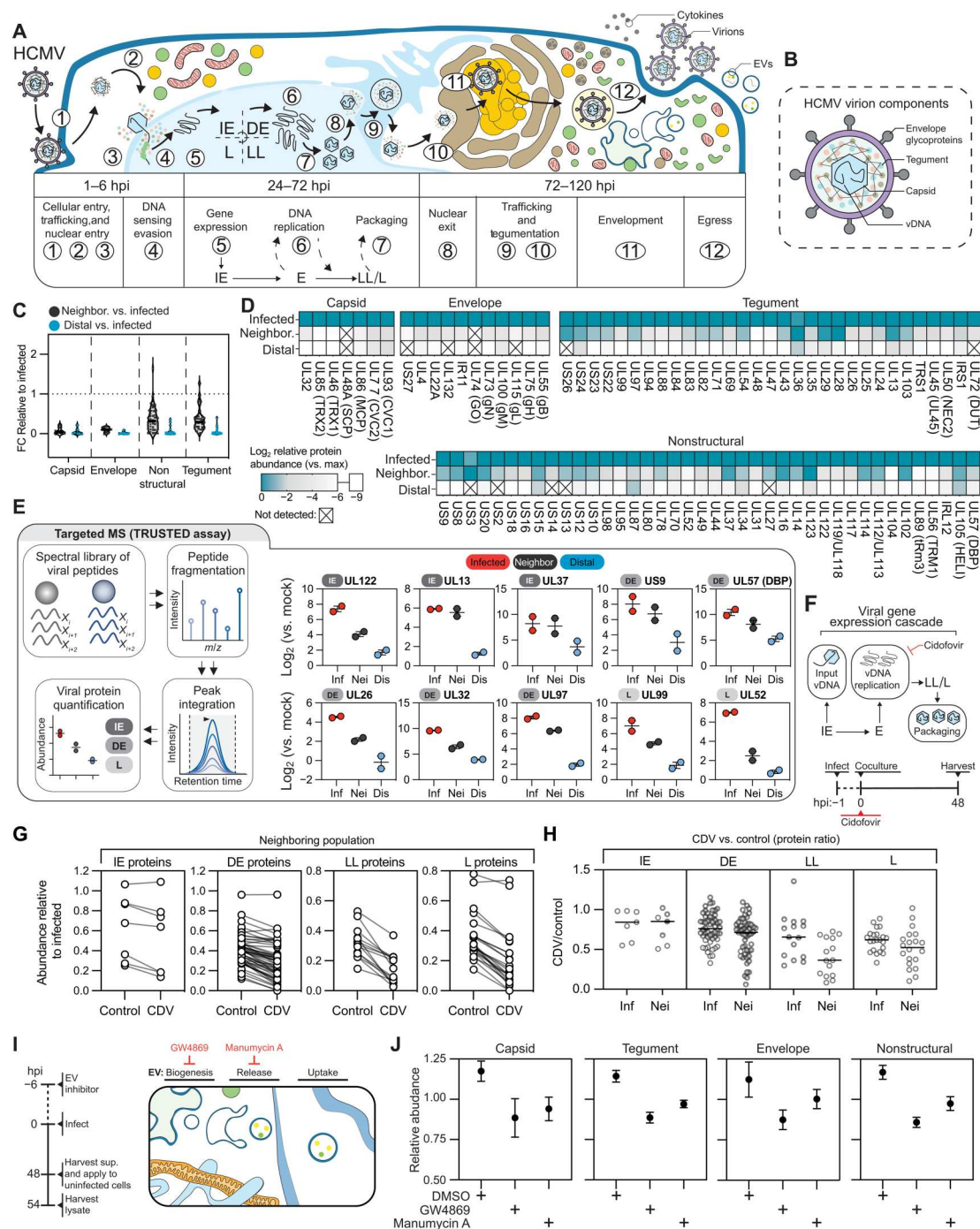


Fig. 2. Viral protein detection in the neighboring cell population. (A) HCMV life cycle. Viral genome release into the nucleus leads to immediate early (IE) gene expression, thereafter activating early (E; or delayed early, DE) gene expression, which initiates viral genome replication and late (L; or leaky late, LL) gene expression. Resulting cytokines, extracellular vesicles (EVs), and infectious progeny virions can spread to neighboring cells. (B) HCMV virion components include envelope, tegument, and capsid proteins. (C) Viral protein abundance fold changes in neighboring or distal, versus infected cells. Proteins categorized by virion component (capsid, envelope, tegument, and nonstructural). (D) Viral protein abundances in infected, neighboring, and distal cells, categorized as capsid, envelope, tegument, and nonstructural. Abundances in each group were normalized to the maximum abundance of all groups. Cross: Undetected. (E) Targeted MS (TRUSTED assay) workflow of HCMV proteins by parallel reaction monitoring (PRM). A spectral library of peptides was generated, and detected peptides were integrated to quantify protein abundances. Peptide abundances were normalized to reference peptide intensities before relative quantification. *n* = 2 biological replicates. DBP, major DNA-binding protein. (F) Model of cidofovir (CDV) inhibition during HCMV infection and VME treatment schema. (G) Viral protein abundances in neighboring cells (\pm CDV), quantified by MS analysis. (H) Viral protein abundance ratios (CDV-treated versus control) in infected and neighboring populations. Proteins categorized by viral temporal expression classes. (I) Treatment schema for EV inhibitors (manumycin A or GW4869) and model of inhibition. (J) Virion component proteins quantified by TRUSTED assay in WT MRC5s treated with supernatant from HCMV-infected MRC5s supplied with an EV inhibitor or dimethyl sulfoxide (DMSO; *n* = 2 biological replicates. Bars: average and 95% confidence interval).

endosomal sorting complex required for transport-I (ESCRT-I), using our previous datasets from thermal proteome profiling of protein complexes during HSV-1 and HCMV infections (fig. S31) (34, 35). We found that herpesvirus infection either promoted or maintained the dynamic assembly of both the ESCRT-I and exocyst complexes, supporting the generation of EVs during herpesvirus infection. Together, it is likely that the proteomic features of the HCMV VME are the result of transmission of viral proteins and mRNA from the infected cell to neighboring cells via EVs. The presence of these viral proteins in the neighboring population may represent a mechanism acquired by the virus to promote the progression of infection.

Proteomes of infected, neighboring, and distal cells are differentially regulated

Turning our attention to the cellular proteomes within the VME, we next analyzed the host proteomes of the infected, neighboring, distal, and mock cell populations (Fig. 3A). The host proteins were color coded in the heatmap to show their relative abundances among the different populations. *K*-means clustering ($k = 6$) was applied to the dataset to group the proteins with similar regulation patterns, and gene ontology (GO) analyses were conducted for each cluster (Fig. 3, A and B).

As expected, up-regulated in infected cells (cluster 1) were proteins belonging to the GO categories of viral genome replication, viral gene expression, RNA transport, and translation (Fig. 3B). Proteins involved in lipid and amino acid metabolic processes were also in this cluster, consistent with the strong metabolic rewiring effect of HCMV infection (20). In addition, proteins related to organelle localization and interactions were identified in this cluster, which included membrane contact site (MCS) proteins. MCS proteins are known to tether organelles in close contact (10 to 30 nm), forming dynamic networks that regulate organelle structure and biogenesis, metabolism, vesicular trafficking, apoptosis, and lipid organization (36). We recently reported that HCMV infection triggers a global up-regulation in MCS proteins, facilitating proviral organelle remodeling events (19). Having noticed that the profile of this protein cluster shows an infected > neighboring > distal/mock trend, we determined whether intercellular signals involving organelle remodeling are transmitted from the infected to the neighboring cells. Specifically, we assessed whether the levels of some MCS proteins become similarly altered in neighboring cells. Hence, we conducted a targeted MS analysis for MCS proteins using our previously developed MCS-PRM assay (19), which quantifies proteins involved in every major organelle-organelle association (Fig. 3C, fig. S4, and table S5). This analysis confirmed our observations from the proteome analyses, showing a trend of infected > neighboring > distal/mock for MCS proteins (Fig. 3D).

Of interest, the subset of MCS proteins elevated in neighboring compared to distal cells suggests a proviral reorganization of organelle-organelle contacts in this uninfected population. MCSs modulated in the neighboring cells included proteins involved in endoplasmic reticulum (ER)-mediated calcium transfer, including voltage-dependent anion channel proteins (VDACs) and inosine 5'-triphosphate receptor type 3 (ITPR3), which has been shown to contribute to the metabolic profile needed for virus production (37). Other proviral membrane remodeling events were also suggested by changes in MCS proteins such as optic atrophy protein 1 (OPA1) and mitofusin 2 (MFN2), which regulate the

mitochondrial fusion/fission balance (38), and acyl-CoA binding domain containing 5 (ACBD5), which aids in ER-peroxisome contacts and plasmalogen lipid synthesis (39). These changes were specific only to a subset of MCS proteins. For example, vesicle-associated membrane protein-associated protein B/C (VAPB), known to be involved in ER-mitochondria tethering, was more similar in abundance to distal cells, and we previously showed that premature tethering of these organelles is antiviral through activation of stimulator of interferon genes protein (STING)-mediated immune signaling (19). Hence, these changes point to an overall preparation of the neighboring cells for promoting virus spread from the original site of infection.

Further suggesting the priming of neighboring cells, another subset of proteins that displayed an intermediate phenotype between the infected and distal/mock cells was formed of proteins related to the organization of the cytoskeleton and ECM (Fig. 4, A to C, and table S6). Similar to infected cells, the neighboring cells displayed lower levels of specific proteins with known links to the cytoskeleton and movement, collagen fibril formation, adhesion, cell-cell junctions, and receptors. These alterations may reflect the reorganization of organelle interfaces and the secretory system in a manner that resembles HCMV-infected cells. As observed for the gap junction protein GJA1, similar relative decreases were detected for the fibronectin protein FN1, focal adhesion complex adaptor protein TGFB11 (transforming growth factor beta 1 induced transcript 1), contactin-associated protein CNTNAP1, thrombospondin protein THBS1, and the integrin ITGA6. Previous studies have shown that HCMV infection of fibroblasts reduces extracellular type I collagen, fibronectin, and proteins involved in intercellular interactions (30, 40). Specifically, focal adhesions involving TGFB11 and connexin junctions involving GJA1 were shown to be disrupted in infected fibroblasts (30). Given that reduced levels of GJA1 were also found on expression of the human papillomavirus 16 E5 protein (41), the dispersion of focal adhesions and cell-cell junctions may represent a strategy to promote virion spread by priming neighboring cells for an infection. Of note, the proteomic features of the neighboring cells were retained in the presence of CDV treatment (as assessed by PCA). Less than 2% of host proteins were significantly different in each VME population between the CDV treated and untreated conditions (fig. S3, D to G, and table S3). These data suggest that the molecular features of the VME derive from protein secretion from the infected cells (e.g., EVs containing viral IE and DE proteins, mRNA) rather than from the progression through an early stage of infection. Collectively, our findings suggest that HCMV infection primes neighboring cells to decrease ECM proteins, which may be a strategy to enhance viral spread to nearby cells, in part, by diminishing physical barriers to infection.

Distal cells, rather than neighboring cells, have up-regulated immune proteins

Having found that neighboring cells exhibit changes that point to proviral remodeling, we had to reconcile the knowledge that infected cells are also known to activate immune signaling and drive the formation of inflammatory foci surrounding the infection site. Hence, we aimed to define the proteomic signatures of distal cells when compared to neighboring cells. The proteins in clusters 2 and 3 exhibited a pattern of distal > neighboring and were further filtered according to statistical significance (268 proteins with $P <$

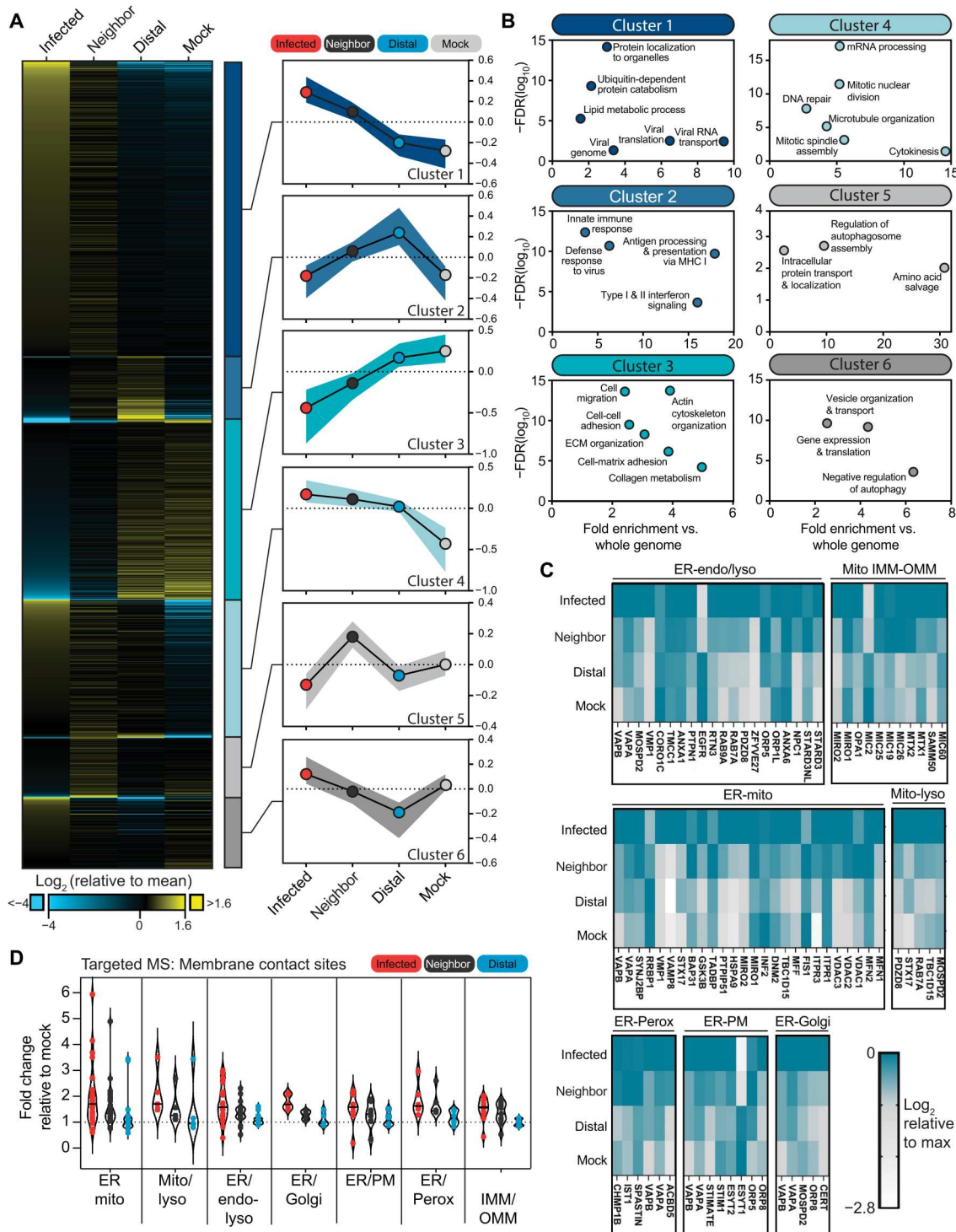


Fig. 3. Proteomes of infected, neighboring, and distal cells are differentially regulated. (A) A total of 5134 host proteins in the heatmap were color coded to show the relative abundance among different populations. Hierarchical *k*-means clustering (by Morpheus, *k* = 6) was applied to the dataset to group the proteins with similar regulation pattern, which were graphed as trend lines displaying the median and interquartile ranges. (B) Gene ontology (GO) analyses were conducted for each cluster. Representative GO terms are labeled in the figure, with fold enrichment and false discovery rate (FDR). MHC I, major histocompatibility complex I. (C) Targeted MS analyses by PRM for all the MCS proteins. Protein abundances in each group were normalized to the maximum abundance of all groups and plotted as \log_2 values. ER, endoplasmic reticulum; endo, endosome; lyso, lysosome; mito, mitochondria; IMM, inner mitochondrial membrane; OMM, outer mitochondrial membrane; perox, peroxisome; PM, plasma membrane. (D) Violin plots of fold change of the protein abundances in the infected, neighboring, or distal group relative to the mock group clustered by organelle:organelle contact type.

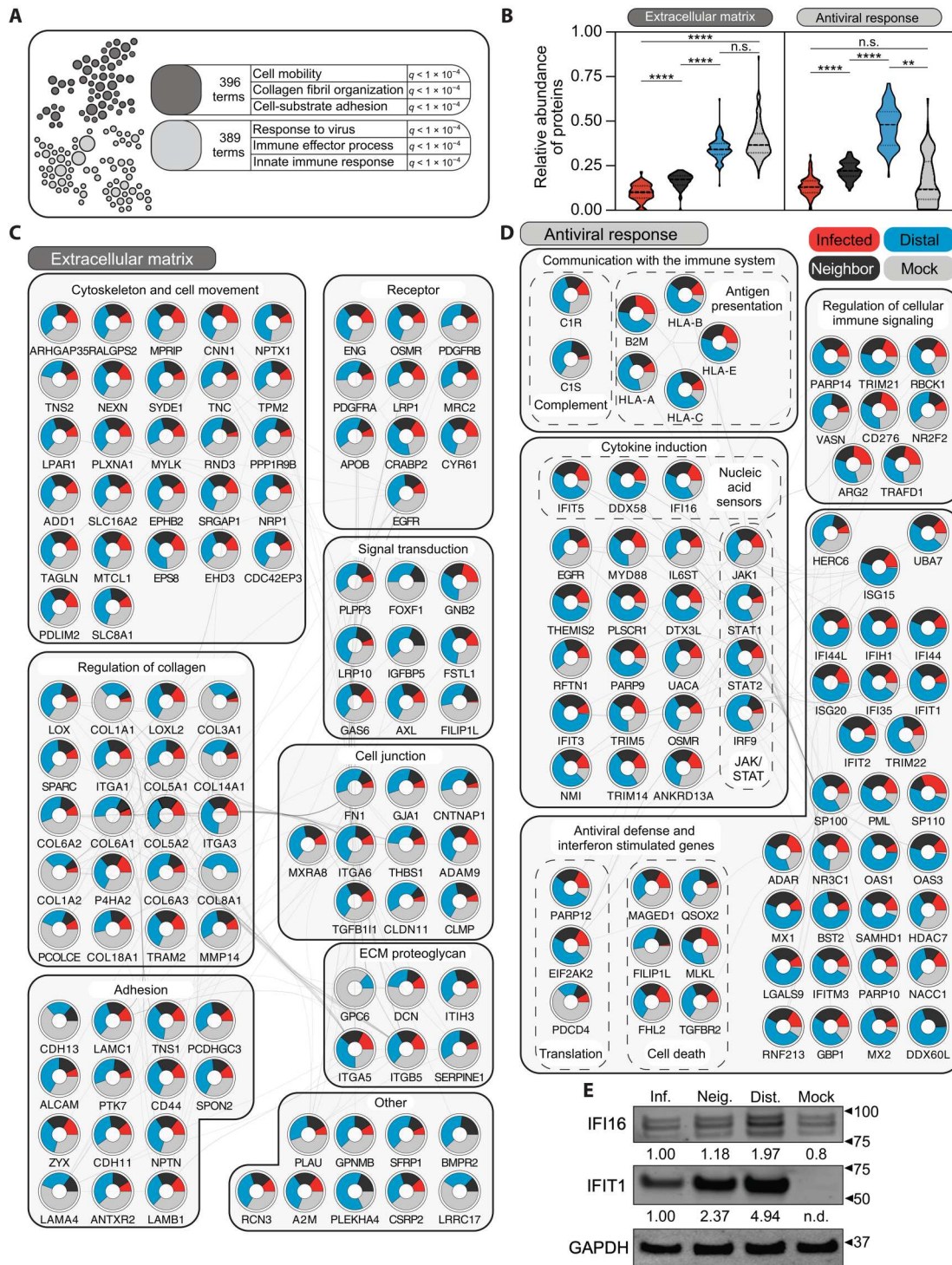


Fig. 4. Immune and ECM proteins are down-regulated in neighboring cells compared to distal cells. (A) Cellular proteins that are down-regulated lower than 0.65-fold in neighboring cells compared to distal cells were filtered by $P < 0.05$. The resulting 268 proteins were submitted for functional module analysis via HumanBase, yielding two networks related to either the extracellular matrix (ECM)/cytoskeleton or the antiviral response. (B) The proteins contributing to two networks in (A) were normalized relative to the sum of each protein. Abundances were graphed on the basis of proximity population. Statistics were by Kruskal-Wallis test (n.s., not significant; $**P < 0.01$; $****P < 0.0001$). (C and D) The 268 significantly different proteins from (A) were additionally manually annotated for functions related to the functional network and then subclustered. (C) Interaction network of proteins from (A) contributing to ECM and cytoskeleton regulation. Nodes are relative abundance based upon cell population (infected, neighboring, distal, or mock). Edges are from STRING. (D) Interaction network of proteins from (A) contributing to the antiviral response. Nodes and edges are as in (C). (E) Validation of IFIT1 and IFI16 protein abundances by Western blot. Western blot images were acquired by Odyssey, and the densitometry was quantified by Image Studio Lite. The quantification results of protein bands (relative to mock) were labeled in the figure. GAPDH, glyceraldehyde-3-phosphate dehydrogenase.

0.05; Fig. 3A). In addition to a functional network containing proteins involved in the organization of ECM and cytoskeleton, the other major resulting functional cluster contained antiviral proteins (Fig. 4). Compared to mock and neighboring cells, the distal cells had up-regulated levels of ISGs (e.g., IFIT1, MX1, and ISG15), nucleic acid sensors (e.g., IFI16, DDX58, and IFIT5), and members of the Janus kinase/signal transducer and activator of transcription (JAK/STAT) signaling pathway downstream of the IFN receptor (Fig. 4, B and C, and table S6). We validated the expression pattern of the ISGs, IFI16 and IFIT1, by Western blot analysis following FACS of the VME (Fig. 4E).

Upon infection, there is a narrow window of opportunity for pattern recognition receptors [e.g., IFI16 and cyclic GMP-AMP synthase (cGAS)] to sense the pathogen and induce the expression of IFNs and cytokines. Paracrine signaling triggers the antiviral response in nearby cells, leading to the expression of ISGs. These data suggest that, despite the cells near the site of primary infection being exposed to cytokines released early during infection, it is the distant cell population that is better primed against future infection. One possibility is that viral infection can more potently induce proteomic changes in nearby cells by delivering viral RNA and proteins via EVs. In the neighboring population, we observe the presence of immunomodulatory viral proteins like pUL37 (Fig. 2), which has been shown to bind TBK1 to abrogate the TBK1-STING-IRF3 interaction and inhibit intrinsic immune signaling (42). Beyond cellular immunity, higher expression of proteins involved in antigen processing and presentation (human leukocyte antigens) and of the complement system suggests that the distal population of cells is primed to communicate with the innate and adaptive immune systems, a key role for fibroblasts in the early immune response to viral infection.

Cells proximal to HCMV infection exhibit mitotic arrest

When investigating the proteomes of cells proximal to infection, we noted that, in comparison to distal cells, these cells exhibited an up-regulation of proteins related to cell cycle control (cluster 4; Fig. 3, A and B, and fig. S5A). This was, in part, expected, as viruses are known to exert control over the cell cycle state of a host cell to promote viral DNA replication (43). HCMV, a nuclear-replicating virus, encodes mechanisms to modulate the host cell cycle to gain access to host DNA replication and repair proteins while also inhibiting cellular DNA synthesis (44, 45). Thus, HCMV replicates at the G₁/S boundary (46). Infected cells within our VME had high levels of certain DNA repair proteins, like replication protein A3 (RPA3) and ataxia telangiectasia mutated (ATM), and low levels of host replicase proteins, like the DNA polymerase delta catalytic subunit (POLD1) (Fig. 5A). However, the neighboring cells displayed an unexpected proteome signature for cell cycle related proteins. Compared to distal cells, neighboring cells had lower levels of cyclin D1 and Cdk6, which could indicate either arrest in G₁ phase or acceleration to S phase, since these factors are known to inactivate pRb and promote S phase entry (47). In conjunction with the observation of higher levels of POLD1, POLA2, Ki-67, and origin recognition complex (ORC) proteins in neighboring cells, these findings point to a possible increase in S phase entry and cell cycle progression. This cell population also had significantly lower ATM levels, a proviral factor that not only is necessary for infection but that also inhibits S phase entry (48). Therefore, our data suggest that proximity to the infected cell promotes cell cycle progression and S phase

entry. However, host S and G₂ phases would inhibit HCMV replication (46). Hence, we expected these observations to be accompanied by additional changes in the cell cycle proteome profile of neighboring cells. We further found higher levels of cyclin B1 and aurora kinases A and B (AURKA and AURKB) in the neighboring versus distal cells, indicating increased entry into mitosis (Fig. 5A). This was coupled to the depletion of components of the anaphase-promoting complex (APC/C) (ANAPC1 and ANAPC4) but high expression of the APC/C adaptor molecules [fizzy-related protein homolog (FZR1) and CDC20]. Together, these proteome alterations suggest that neighboring cells are coaxed to enter the cell cycle and may potentially have accelerated kinetics through the cell cycle checkpoints. In addition, inactivation of the APC/C may halt the cell cycle progression to promote accumulation of neighboring cells in mitosis.

These observations of changes in cellular protein abundances related to the modulation of the cell cycle are also in agreement with our above-mentioned detection of selected viral proteins in neighboring cells. Both pUL82 (pp71) and pUL97 have been reported to promote cell cycle progression and support viral genome replication (49, 50). To further confirm our proteomic findings, we repeated the VME experiment, searching specifically for checkpoint proteins, proteins that mark cell cycle transitions, and protein representing mitotic processes (Fig. 5L and fig. S5, B and C). Confirming our proteomic observations, G₁ arrest proteins were diminished in neighboring cells including the canonical G₁/S checkpoint protein, p21 (Fig. 5L and fig. S5, B and C). Concurrently, S phase markers (proliferating cell nuclear antigen and Ki-67) and M phase progression makers (CCNB1 and AURKB) were elevated (Fig. 5L). Last, proteins associated with mitotic chromatin condensation (condensin complex subunits NCAPG and NCAPD2) and centromere formation INCENP (inner centromere protein) were elevated in neighboring cells versus both infected and distal cells (fig. S5, B and C). Together, these data suggest that cells in close physical proximity to an HCMV-infected cell accelerate through the cell cycle and may be arrested in M phase.

To validate the model derived from the proteome analyses, we next directly interrogated the cell cycle state of cellular populations within the HCMV VME by adapting a flow cytometry-based assay (Fig. 5, B to E) (51). The GFP and mCherry fluorescent marks used to distinguish infected, neighboring, and distal cells within the VME were supplemented with three other fluorescent channels to mark different cell cycle stages (Fig. 5, B and C). Mitotic cells were identified by Phycoerythrin-Cyanine7 (PE-Cy7)-labeled phosphorylated histone H3 Ser10 (pH3-Ser10; Fig. 5, B and D). In nonmitotic cells, S phase cells were identified by a positive signal of 5-ethynyl-2'-deoxyuridine (EdU) incorporation, marked by a click chemistry reaction with azide-AF647. The G₁ and G₂ phase cells were identified by assessing 2N and 4N DNA amounts, as indicated by DAPI (4',6-diamidino-2-phenylindole) staining (Fig. 5, B and E). Our findings show clear differences between each population of cells in the VME that are consistent with our proteomics findings (Fig. 5, F to K).

Both infected cells and the neighboring population had decreased levels of G₁ phase (Fig. 5, F and H). However, the infected population displayed stunted EdU intensity compared to either the neighboring or distal cells (Fig. 5E). This observation is consistent with the viral strategy to block host DNA replication, and this EdU signal is likely from viral replication and not representative of true S

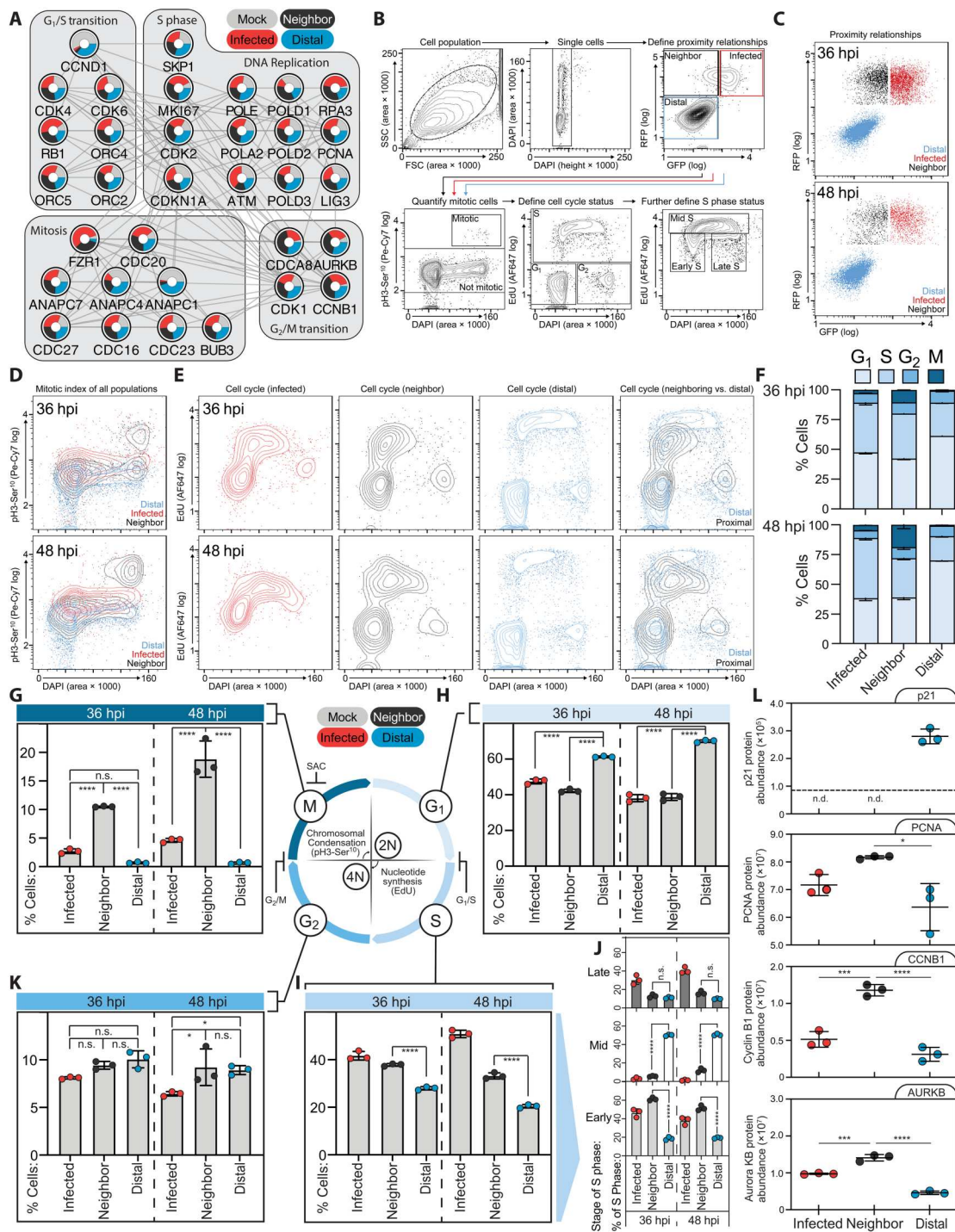


Fig. 5. Cells that neighbor HCMV infection show increased cell cycle kinetics and are arrested in mitosis. (A) VME data were searched for proteins contributing to cell cycle progression or regulation and represented as an interaction network clustered by cell cycle stages. Nodes and edges are as in Fig. 4. (B) Flow cytometry-based cell cycle profiling workflow. Cells were sorted by FSC and side scatter (SSC) and then by DAPI (4',6-diamidino-2-phenylindole) width and area. Cell proximity relationships were sorted by mCherry and GFP expression. Mitotic cells were determined by pH3-Ser10 phosphorylation (PE-Cy7). Cell cycle stages were determined by 5-ethynyl-2'-deoxyuridine (Edu) incorporation (AF647) and DAPI. S phase profiles were determined by Edu and DAPI levels. (C to E) Representative dot plots of cell proximity populations (C). Representative contour plots (5%) of mitotic index (D) and cell cycle analysis (E) of each cell population. Top is coculture for 36 hours, and bottom is coculture for 48 hours. *n* = 3. RFP, red fluorescent protein channel, indicating mCherry intensity. (F) Summary analysis of cell cycle distributions for each proximity population. Error bar, SD. *n* = 3. (G to K) Quantification of (D) and (E) demonstrate significant changes in cell cycle phases. Error bar, SD. **P* < 0.05; *****P* < 0.001; ******P* < 0.0001. Edu labeling indicates DNA synthesis; however, HCMV DNA is synthesized in the infected cells, leading to the positive signal in Edu labeling. Thus, the S phase quantification in the infected cells is not applicable. (L) A separate VME MS/MS analysis was performed to validate cell cycle proteomic findings. Shown are abundances of proteins related to G₁/S transition. Error bar, SD. *P* values are as in (G) to (K). n.d., not detected.

phase. On the other hand, neighboring cells had a higher level of S phase compared to distal cells (Fig. 5I). Close examination revealed that the S phase profile in this neighboring population is more typical of cells in early S phase, with relatively low DAPI content and EdU signal (Fig. 5J). Conversely, the distal cells had a typical S phase profile, with most S phase cells in processive S phase with an intermediate ploidy and high levels of EdU incorporation. These findings are consistent with the observation that neighboring cells had decreased levels of cell cycle checkpoint proteins (e.g., ATM and PML) and high levels of early S phase proteins (e.g., origin licensing factors, ORC) (Fig. 5A).

Further examining the cell cycle profile of the VME revealed that the G₂ checkpoint was not differentially activated between neighboring and distal cells (Fig. 5K). However, compared to either the infected or distal population, the neighboring cells displayed a notable increase in pH3-Ser10 levels in the 4N population, indicating elevated mitosis (Fig. 5, D and G). This observation concurred with our finding that neighboring cells had higher levels of cyclin B1, AURKA and AURKB, which promote M phase entry. Notably, the neighboring population displayed decreased levels of G₁ phase cells that were proportional to the elevated levels of S and M phase cells, but the G₂ population was not changed relative to the distal population. This indicates that the increase in M phase cells was not due to inactivation of the G₂/M checkpoint but rather due to impaired progression through mitosis in cells proximal to infection. Visual assessment via microscopy showed that pH3-Ser10-positive cells in the neighboring population of cells showed evidence of chromatin condensation indicative of mitosis (fig. S5D).

By expanding our cell cycle analysis to two time points following infection, we observed that there was an increase in neighboring cells undergoing mitosis from 36 to 48 hpi (Fig. 5G). This was not complemented by an increase in G₁ phase cells (Fig. 5H). Together, our results demonstrate that neighboring cells exhibit accelerated kinetics through the cell cycle checkpoints and become M phase arrested.

Cells proximal to primary infection are more susceptible to secondary infections

Together, our characterization of the VME suggests that lines of communication between the infected and neighboring cells trigger a series of changes that may increase the susceptibility of neighboring cells to subsequent viral infections. Neighboring cells seem to exhibit alterations in intracellular organization (e.g., changes in MCS proteins), cell-to-cell communication (e.g., ECM, cell junction, and adhesion proteins), and dampened antiviral response (e.g., immune signaling and ISG proteins). In addition, the neighboring population displays an abnormal cell cycle profile. However, instead of an arrest in G₁ phase, which is the cell cycle phase that supports HCMV IE gene expression and replication, we discovered an increased accumulation in M phase. This cell cycle profile may also affect the resistance of neighboring cells to secondary infections, given the known suppression of DNA sensors and transcription during mitosis (52).

To understand whether the molecular features of cells in the HCMV VME prime subsequent rounds of infection, we tested the response of these cells to secondary infections. Using a confocal microscopy-based superinfection assay within a VME context, we first tested responses to a new round of HCMV infection (Fig. 6A). The VME was established using SP-TATκ-mCherry fibroblasts infected

with UL32-GFP-HCMV, which were then cocultured with WT fibroblasts at two different ratios (1:3 and 1:10; infected:WT cells) to alter the frequency of neighboring cells. Thirty-six hours later, the coculture was infected with WT HCMV (MOI of 1). Immunofluorescence (IF) microscopy was used to detect IE1-positive cells in a GFP-negative background, indicating that these cells were infected by the WT HCMV but not by the GFP-HCMV used to establish the primary infection. We next calculated the occurrence of neighboring cells (GFP⁻ and mCherry⁺) and distal cells (GFP⁻ and mCherry⁻) that were infected with WT HCMV (IE1⁺). Our results showed that a higher portion of neighboring cells (i.e., cells in proximity to the primary infection) were infected on secondary challenge compared to the distal subpopulation (Fig. 6, B and C). In addition, with a secondary HCMV challenge of the CDV-treated VME, we also found higher percentage of infected cells in the neighboring population (fig. S6, A and B), demonstrating that the higher infected percentage of neighboring cells is not due to the spread of primary infection. One explanation for this higher infection rate in neighboring cells is that the neighboring cells have been primed to have increased susceptibility to subsequent rounds of HCMV infection despite being more likely to receive danger signals produced by the primary infected cell.

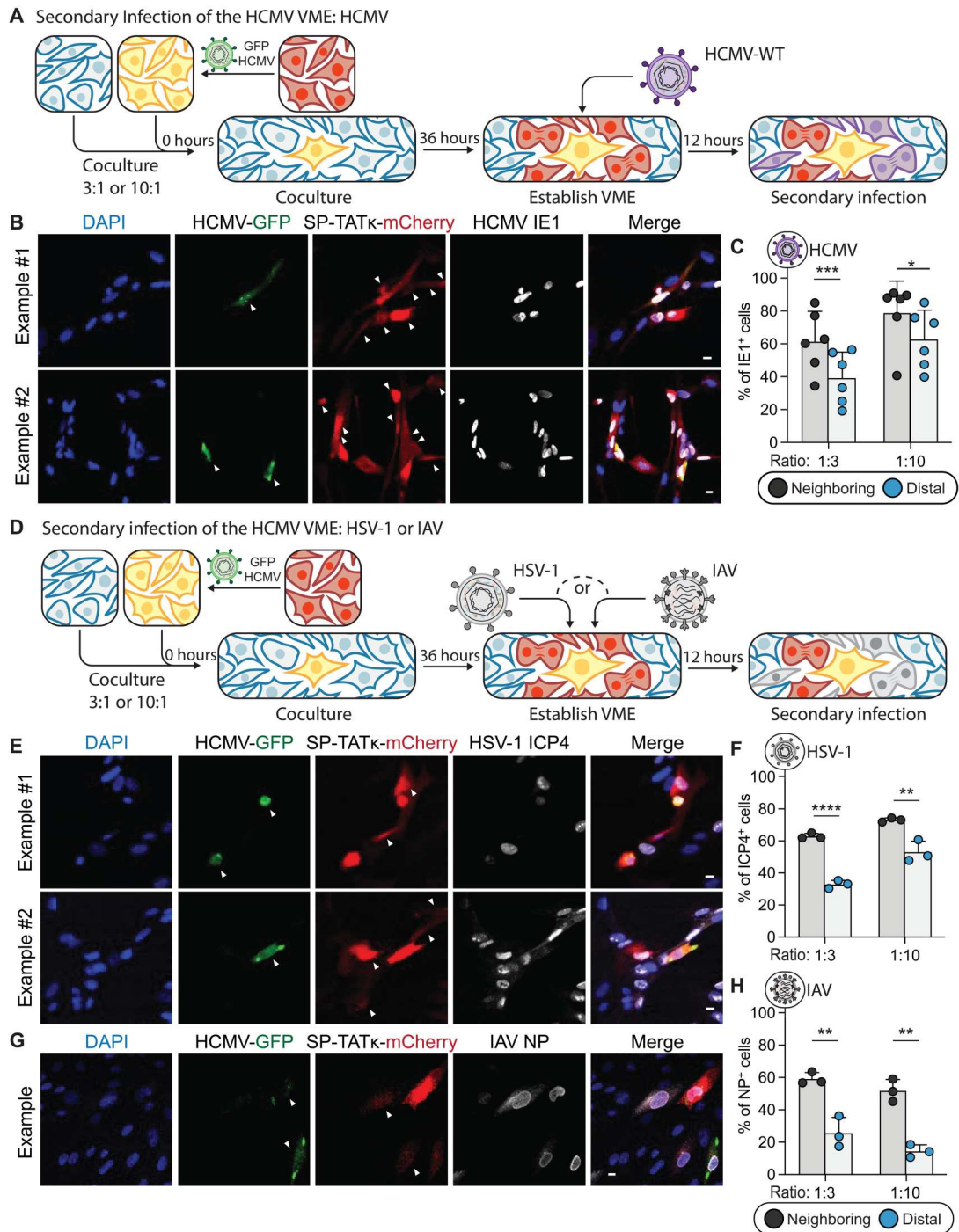
Given the ancient history of coevolution between HCMV and humans, it stands to reason that the virus may have acquired mechanisms to promote its spread in tissues via manipulation of uninfected cells. The virus encodes interleukin-10 homologs (UL111A) that are known to dampen immune responses to the virus (53). Our findings uncover additional means through which HCMV primes neighboring cells for infections. Given the broad tissue tropism of HCMV and its ability to reactivate during periods of immunosuppression throughout an individual's life span, the likely incidence of secondary infections with a range of human viruses is high. However, it is not clear whether the changes that are promoted by HCMV in neighboring cells are specific to only promoting secondary infections with HCMV or whether these alterations have a broader effect on secondary infections with other viruses. To answer this question, we used the secondary infection model described above to test infections with HSV-1 and IAV. These two viruses were selected to represent a similar, nuclear-replicating herpesvirus but with a shorter replication cycle of under 24 hours (HSV-1) and a nuclear-replicating RNA virus (IAV) (Fig. 6D). Our secondary infection assay revealed that cells that neighbor the initial HCMV infection are more susceptible to both HSV-1 and IAV infections (Fig. 6, E to H). Collectively, our results demonstrate that the primary virus infection reshapes the local microenvironment through intercellular communication and that the spatial address of cells within this VME guides the relative susceptibility to secondary infections.

DISCUSSION

The spatial and temporal definitions within a VME have remained an unmet need toward understanding viral pathobiology and spread between cells. To begin to address this gap, here, we characterized the molecular hallmarks underlying how an infection influences intra- and intercellular communication surrounding infected cells based on the proximity to infection. Insight into these characteristics is essential for establishing the principles that govern the control of cell-to-cell communication, which has long-term implications

Fig. 6. Neighboring cells show higher susceptibility to secondary infection compared to distal cells.

(A) Workflow of the secondary infection assay to determine susceptibility to secondary HCMV infection. After coculturing SP-TATκ-mCherry/GFP-HCMV and WT MRC5 cells for 36 hours, the microenvironment was challenged with a secondary infection by WT HCMV. Twelve hours later, cells were fixed and stained for IE1. Secondary infection of neighboring cells was quantified as mCherry⁺, GFP⁻, and IE1⁺. Secondary infection of distal cells was quantified as mCherry⁻, GFP⁻, and IE1⁺. **(B)** IF images showing two representative views of HCMV secondary infection assay. Arrows indicate GFP⁺ or mCherry⁺ cells. Scale bars, 10 μm. **(C)** Quantification of HCMV secondary infection IF data for coculture ratios of 3:1 or 10:1 (WT versus SP-TATκ-mCherry/GFP-HCMV MRC5 cells) for *n* = 6 biological replicates. Error bar, SD. **P* < 0.05; ****P* < 0.001. **(D to H)** (D) Workflow of the secondary infection assay to determine susceptibility to secondary infection by either HSV-1 or IAV. After 36 hours of coculture, the microenvironment was challenged with a secondary infection by either HSV-1 or IAV and then stained 12 hours later for ICP4 (HSV-1) or nucleoprotein (NP) (IAV). Secondary infection of neighboring cells was quantified as mCherry⁺, GFP⁻, and either ICP4⁺ or NP⁺. Secondary infection of distal cells was quantified as mCherry⁻, GFP⁻, and either ICP4⁺ or NP⁺. **(E)** and **(G)** IF images showing representative views of the HSV-1 (E) or IAV (G) secondary infection assay. Arrows indicate GFP⁺ or mCherry⁺ cells. Scale bars, 10 μm. **(F)** and **(H)** Quantification of HSV-1 (F) or IAV (H) secondary infection IF data for coculture ratios of 3:1 or 10:1. For each virus, *n* = 3 biological replicates. Error bar, SD. ***P* < 0.01; *****P* < 0.0001.



for understanding the regulation of coinfections, secondary infections, virus reactivation from latency, and diseases resulting from these infections. Thus, we adapted and designed a workflow for spatially discriminating and isolating cells within a VME. From VME sites, we labeled and enriched for subpopulations of primary infected, neighboring, and distal cells. Comparisons to uninfected (i.e., mock-infected) cells enabled us to establish that infection influences

cell features across several levels of spatial proximity. We found that cells that neighbor the site of primary infection contain selected viral proteins, reflecting a viral influence upon this neighboring population. We further discovered that distal cells, rather than neighboring cells, have elevated levels of antiviral and immune signaling markers. While this may initially seem counterintuitive, this observation agrees with the accumulating understanding that virus-

infected cells communicate to adjacent cells via EVs to inhibit immune signaling and promote the spread of infection. These findings also highlight the power of our VME characterization to distinguish nuanced cellular features based upon spatial proximity. Last, we found that cells that neighbor the primary infection are triggered to progress through the cell cycle and arrest in mitosis, despite a preference for G₁ phase for HCMV replication. In addition to proteomic and cell cycle characterizations of each VME cell subpopulation, we establish a functional consequence of cell position upon secondary virus infections. We establish enhanced susceptibility to several secondary infections with nuclear-replicating viruses in the cells neighboring the HCMV primary infection. Our findings indicate that the spatial address of a cell within an infection site guides cell fates by dictating protein expression patterns, cell cycle progression, and susceptibility to secondary infections (Fig. 7).

There are several tempting explanations for the observation that neighboring cells exhibit higher susceptibility to secondary virus infections than distal cells. First, from our differential proteome analyses, lower ISG levels indicate that antiviral defenses are more restricted in neighboring cells, which may be in part due to the presence of viral proteins that inhibit IFN signaling pathways. This result is consistent with previous findings that viral proteins can exist in EVs of HCMV-infected cells (8–10) and viral mRNA can be present in exosomes after infection with the related herpesvirus, HSV-1 (7). Among the viral proteins that we detected in the neighboring cells, several have reported immune-antagonistic roles (e.g., pUL37, pUL82, and pUL83) and thus could contribute to the decreases in host immune protein abundances. Second, lower levels of ECM and cell adhesion proteins suggest that ECM remodeling may occur in neighboring cells, reducing the physical barrier for the viral entry. Third, higher levels of MCS proteins were found in neighboring cells, which correlated to changes in the cytoskeleton proteins in this population. Given knowledge that ER-organelle contacts, such as with mitochondria and peroxisomes, support virus production (19), increased MCS proteins may serve to prime neighboring cells for the metabolic needs of infection. In

addition, a summed effect of these possibilities may be occurring, which could explain otherwise unexpected signatures of each VME cell population. For example, although HCMV receptor EGFR levels in neighboring cells were higher than those in infected cells, as expected, given EGFR internalization and degradation following virion entry in infected cells, they were lower than those in distal or mock cells. In comparing neighboring to distal cells, it is thus intriguing to reconcile the lower EGFR levels with the increased susceptibility to an infection. One possible explanation is that the levels of the EGFR remaining are sufficient to sustain HCMV entry. Concurrent to lower EGFR levels, the summed effect of the altered levels of proteins involved in innate immunity, ECM, and the cell cycle may have a more significant impact on susceptibility.

In the neighboring population, we also observed a higher percentage of S phase and mitotic cells. This was unexpected given that HCMV infection is tied to G₁ phase, although the virus also uses cellular S phase proteins (46). HCMV infection induces the degradation of cyclin A as a mechanism to decouple the expression of S phase proteins from the replication of the host genome (45). There are several possibilities to explain this phenomenon in neighboring cells. This may be a wound-healing response driven by the down-regulation of the ECM proteins (54). Conversely, the down-regulation of the ECM proteins could be a consequence of cells entering S phase and mitosis, which decreases anchoring (55). Another explanation is that most cells in tissue are terminally differentiated and in G₀ phase. Viral manipulation of uninfected, neighboring cells represents an opportunity to overcome a rate-limiting step in chromatin remodeling that leads to the expression of host S phase proteins and thus hasten subsequent rounds of infection. Supporting this notion, pUL97 and pUL82 were found in neighboring cells. These viral proteins could accelerate S phase entry given their capacity to activate the E2F family of transcription factors and inactivate the pocket protein family of tumor suppressors (49, 50, 56). S phase entry is also regulated via the activity of the mitotic APC/C adaptor, Cdh1 (FZR1) [reviewed in (57)], which is

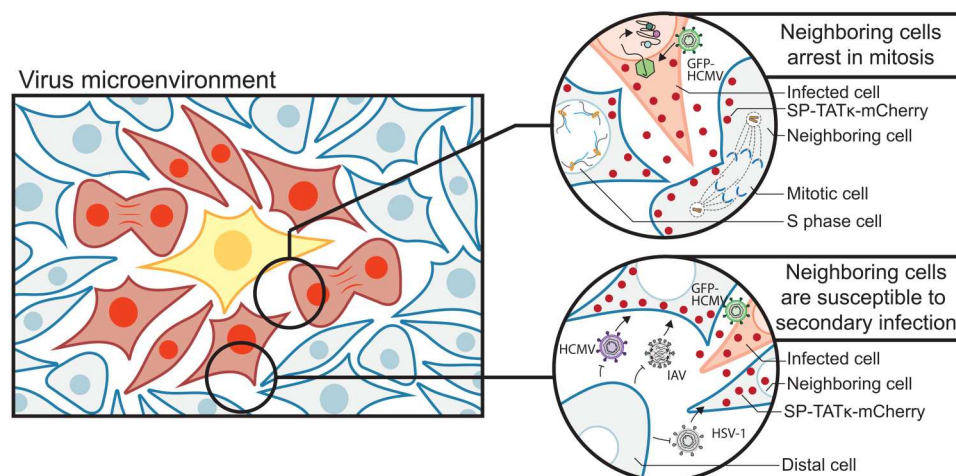


Fig. 7. Model of the HCMV viral microenvironment. To generate a VME system, SP-TAT κ -mCherry-expressing fibroblasts were infected with GFP HCMV and subsequently cocultured with uninfected WT fibroblasts. Neighboring cells were labeled through secretion of the cell-permeable SP-TAT κ -mCherry by the infected cells. Proteomic profiling, cell cycle analysis, and viral susceptibility assays were performed to quantify features of the VME based on proximity to HCMV infection. Cells that neighbor HCMV infection were found to progress through the cell cycle and arrest in mitosis. Neighboring cells are primed for secondary infection by either HCMV or other nuclear replicating viruses, exhibiting increased susceptibility in comparison to distal cells.

inhibited by the HCMV kinase, pUL97, and phosphatase, pUL21a (56). We found that ANAPC1 and ANAPC4, both pUL21a targets, are degraded in neighboring cells, which may contribute to the mitotic arrest observed in this population.

Conceptually, mitotic cells should not support viral replication, given that cellular chromatin is condensed and the nuclear envelope can be disrupted. Mitotic entry of HCMV-infected cells decreases viral replication and induces cell death via chromosomal abnormalities (58). Thus, it is not clear whether the mitotic population in neighboring cells contributes to the susceptibility of this population to secondary infection. One possibility is that HCMV has acquired the capacity to induce M phase-arrested cells to prepare cells for entering G₁ phase. Another possibility is that the neighboring cells are arrested in mitosis before the disruption of the nuclear envelope. A final possibility is that neighboring cells undergo a prolonged mitotic arrest, followed by completion of mitosis without activation of the APC/C:Cdh1 complex. An emerging concept in oncogenic transformation is the role of APC/C:Cdh1 to maintain genomic stability by regulating DNA replication and cell division (57). Disruption of these proteins can lead to genomic instability and aneuploidy and are associated with cancer (59). In the context of HCMV-linked disease, disruption of cell cycle regulation in cells that are proximal to the site of infection may be linked to the growing recognition of HCMV as an oncomodulatory virus (17). Supporting this possibility is the observation of abnormalities in centrosome duplication and spindle assembly formation linked to HCMV infection-induced pseudomitosis (60). In further agreement with this notion is evidence of binucleation in conventional viral infections at low MOIs, which may be a consequence of mitotic dysregulation or an increased rate of viral oncogene-induced genomic instability.

In assessing cell populations from within a VME, an important consideration was the extent to which the observed molecular signatures of infection-adjacent cells were either the result of uptake of soluble mediators expressed by infected cells or the result of an early-stage nascent infection. In support of the former possibility, our findings indicate that (i) viral capsid and envelope proteins are barely detected in neighboring cells; (ii) viral genomic DNA is barely detected by qPCR in either neighboring or distal cells; (iii) the overall proteomes of CDV-treated cells are identical within each VME cell population by PCA; (iv) CDV-treated cells exhibit the same trends in proteome changes for ECM and antiviral response proteins as well as superinfection susceptibility; and (v) treatment with EV inhibitors reduced all temporal classes of viral proteins, suggesting that EVs contribute to establishing the presence of HCMV IE and DE proteins in neighboring cells. Collectively, these findings suggest that the observed proteome changes are not being driven by nascent infection but rather by the presence of viral proteins and soluble mediators taken up by the neighboring cells.

Together, our study brings to light the molecular complexities governing inter- and intracellular communication within a VME. Our findings form the foundation for how a virus infection reorganizes the surrounding cellular environment in a proximity-dependent manner. The result of this intracellular signaling is the concurrent virus-directed spread of an infection and host engagement of community-level defenses. Because the labeling strategy was originally established to study the tumor microenvironment, our adapted workflow to interrogate the VME can be further

applied as a multimodal framework to study other virus or infection context. This includes infection with viruses expressing other fluorescent tags (e.g., blue fluorescent protein), virus reactivation from latency, virus spread across multiple replication cycles, virus spread between different cell types, and during specific stages of infection. A relevant consideration is the labeling radius and photostability of the current SP-TATκ-mCherry labeling approach. SP-TATκ-mCherry cells were observed to label approximately five cell layers in vivo (14). The fluorescent protein was shown to have an intracellular half-life of 43 hours with reported retention of high fluorescence intensity due to its high photostability and ability for reuptake by cells. Upon testing coculture incubation periods of 24, 48, and 72 hours, we observed VME sites at all time points. The time point upon which we observed that mCherry labeling efficiency was optimal in providing an adequate ratio of labeled and unlabeled cells was 48 hours. Thus, future investigations could consider optimizing the approach to enable adequate labeling at earlier time points (e.g., shorter than 24 hours). This is relevant not only for understanding the microenvironment effects during early stages of an infection but also for the ability to study the VME of faster replicating viruses. We also anticipate that the proximity-dependent alterations that we observed in a two-dimensional culture system will be dynamically magnified in the complex environment of host tissue. Thus, to further investigate the VME, we envisage that this experimental platform has exciting potential to integrate with the emergence of sensitive single-cell technologies (e.g., single-cell RNA sequencing and proteomics), three-dimensional culture systems (e.g., spheroids and organoids), coculture approaches, and in vivo models. Inactivation of canonical secretory and receptor-mediated signaling pathways in a VME context will be valuable to determine their contributions to observed secondary infection susceptibilities. Given the developing knowledge of extensive heterogeneity among cells during virus infections, it will be interesting to examine the extent of heterogeneity within each VME cell subpopulation. Such investigations would enable the tracking of individual cell trajectories and fates in a VME with high spatial and temporal resolution.

MATERIALS AND METHODS

Tissue culture

MRC5 primary human fibroblasts (the American Type Culture Collection) were cultured at 37°C with 5% CO₂, in Dulbecco's modified Eagle's medium (Life Technologies) supplemented with fetal bovine serum (10% v/v), penicillin (100 U/ml), and streptomycin (100 mg/ml) (Gibco).

SP-TATκ-mCherry cell line

To generate the SP-TATκ-mCherry construct, forward and reverse sequences of SP and TATκ were synthesized, flanked with up- and downstream restriction sites (Integrated DNA Technologies). After annealing and restriction digestion, SP-TATκ was ligated with mCherry on pLEX-MCS plasmid (Thermo Fisher Scientific).

The SP-TATκ-mCherry MRC5 cell line was generated by lentiviral transduction. The pLEX-SP-TATκ-mCherry plasmid was cotransfected with lentiviral packaging vectors VSV-G and ps-PAX2 into human embryonic kidney 293T cells, with a ratio of 1:1:1.5. Lentiviruses were collected at 48 and 72 hours after transfection and filtered with 0.45-μm membranes. WT MRC5s were transduced

Allowed modifications were oxidation on methionine; deamination on asparagine; phosphorylation on serine, threonine, and tyrosine; acetylation on lysine; and static carbamidomethylation on cysteine. Peptide spectrum matches were assembled into peptide and protein identifications with a false discovery rate (FDR) of less than 0.01 at both the peptide and protein levels. Proteins with at least two unique peptides identified were quantified, and the peptide abundances were normalized to the total peptide amount.

Targeted MS analysis for HCMV proteins and MCS proteins by PRM

A total of 30,000 cells of the infected, neighboring, distal, and mock cell populations in each biological replicate were collected, and MS samples were prepared as stated above. The HCMV and MCS proteins and the peptides for quantifying these proteins of interest were selected as previously described (19). Peptides analyzed PRM were separated by nano LC-MS/MS with a Q Exactive HF Hybrid Quadrupole-Orbitrap instrument (Thermo Fisher Scientific) using the PRM method. One microgram of peptides was injected in 2 μ l and separated with a linear gradient from 3 to 30% B of 60 min at a flow rate of 250 nl/min on an EASY-Spray PepMap RSLC C18 column (2 μ m, 100 \AA , 75 μ m, and 50 cm) heated to 50°C. MS1 scans (used for normalization) were acquired at a resolution of 15,000, an AGC target of 3×10^6 , a maximum IT of 25 ms, and a scan range of 350 to 1800 m/z and recorded in profile. Twenty PRM methods followed the MS1 scan, and were acquired at a resolution of 120,000, an AGC target of 5×10^5 , a maximum IT of 200 ms, a loop count of 1, spectral multiplexing (MSX) isochronous IT turned on, and an isolation window of 1.2 m/z , and the data acquired in profile. Because this PRM panel monitored 207 peptides, the panel was split into three separate scheduled PRM methods using the above settings. Thus, 69 peptides were monitored in each method to ensure as few overlapping transitions as possible, and all peptides were fragmented with a default NCE of 27. Label-free quantification methods of the peptides were designed and analyzed on Skyline. Peak area of the top three transitions per peptide was used for quantification. Each peptide abundance value was normalized to control peptide intensities for each sample. For heatmaps, ratios were plotted of the protein abundance of each sample relative to the max abundance of the protein among all samples.

Bioinformatics and functional pathway analysis

Host proteins were clustered by \log_2 abundance normalized to the mean value. Clustering was performed using Morpheus from the Broad Institute (k -means clustering with $k = 6$ and 1000 maximum iterations). For GO biological process analysis, gene names of the proteins from each cluster were submitted to the PANTHER classification system. Statistical overrepresentation tests were performed for each protein cluster using the GO biological process complete annotation dataset. Functional networks of protein-protein interactions were generated by Cytoscape (version 3.8.2) with the ReactomeFI Plugin.

Small-molecule treatments

For inhibiting viral genome replication, CDV was dissolved in PBS and used at 1 μ M. A stock of 2 mM CDV was stored at -80°C . For EV inhibition, GW4869 is used at 10 μ M and stored at 2 mM. Manumycin A was used at 500 nM and stored at 500 μ M. Both EV

inhibitors were dissolved in dimethyl sulfoxide (DMSO) and stored at -20°C .

TUNEL assay

TUNEL (terminal deoxynucleotidyl transferase-mediated deoxyuridine triphosphate nick end labeling) staining was conducted using the In Situ Cell Death Detection Kit TMR Red (Sigma-Aldrich). MRC5 cells in a 12-well plate were treated with 0.5% DMSO, 10 μ M GW4869 + 0.5% DMSO, or 500 nM manumycin A + 0.5% DMSO for 48 hours. Cells were detached by trypsinization and fixed with 4% PFA in PBS for 15 min at room temperature and pelleted by centrifugation at $800 \times g$ for 5 min. Fixed cells were permeabilized with 0.1% Triton X-100, 0.1% sodium citrate in PBS for 2 min at 4°C, and washed with PBS for 5 min. Samples were then stained with 25 μ l of TUNEL mix for 1 hour at 37°C in the dark. For the positive control, samples were treated with deoxyribonuclease I (DNase I) before adding the TUNEL mix. For the negative control, no enzyme solution was added. Cells were then stained with DAPI (0.1 μ g/ml) for 10 min and washed with PBS. Flow cytometry analyses were conducted using BD LSR II flow cytometer (BD Biosciences), and data were analyzed in FlowJo to quantify TUNEL-positive cells.

SDS-PAGE and Western blotting

Cells were lysed in 1 \times Novex NuPAGE LDS Sample Buffer (diluted from a 4 \times stock; Invitrogen) and boiled at 95°C for 10 min. Following bicinchoninic acid (BCA) measurement of protein concentration (Pierce BCA Protein Assay Kit, Thermo Fisher Scientific), 3 μ g protein was loaded per lane. Proteins were separated by SDS-polyacrylamide gel electrophoresis (SDS-PAGE) using tris-glycine gels (10%). Proteins were transferred from the SDS-PAGE gels to polyvinylidene difluoride membranes by the wet transfer method, blocked with 5% (w/v) milk in PBS, and incubated with primary and secondary antibodies. Three 10-min wash steps were performed after each antibody incubation. Protein bands were detected and quantified using a LI-COR Odyssey Imaging System (LI-COR Biotechnology). Primary antibodies used were as follows: mouse anti-IFI16 (1:1000; Santa Cruz Biotechnology, 1G7), rabbit anti-IFIT1 (1:1000; Cell Signaling Technology, D2X9Z), rabbit anti-glyceraldehyde-3-phosphate dehydrogenase (GAPDH; 1:5000; Cell Signaling Technology, D16H11), and mouse anti- α -tubulin (1:5000; Sigma-Aldrich); and mouse monoclonal antibodies against HCMV proteins from T. Shenk: anti-IE1 (1B12; 1:500), anti-UL26 (7H1-5; 1:500), and anti-UL99 (10B4; 1:500). Secondary antibodies used were as follows: goat anti-mouse immunoglobulin G (IgG), Alexa Fluor Plus 800 (1:10,000; Life Technologies), and goat anti-rabbit IgG, Alexa Fluor 680 (1:10,000; Life Technologies).

Flow cytometry-based cell cycle assay

To mark S phase cells exhibiting DNA replication, 10 μ M EdU (Thermo Fisher Scientific) was added into cell culture media 1 hour before sample collection. Cocultured VME cells were trypsinized, fixed with 4% PFA, washed with wash buffer (1% fetal bovine serum in PBS), and pelleted at $800 \times g$ for 8 min. Cells were permeabilized with 0.25% Triton X-100 in PBS; washed and pelleted; and then stained with GFP-488 antibody (1:250; Thermo Fisher Scientific), azide-647 (Click Chemistry Tools), biotinylated PH3-Ser10 antibody (1:100), and streptavidin-PE-Cy7 (1:100) for 1 hour each. Washing and pelleting steps were performed after

each staining. Specifically, the azide-647 staining solution (2 ml in total) contained 10 μ l of 2 mM azide-647, 40 μ l of 100 mM CuSO₄, 40 μ l of 500 mM sodium ascorbate, and 1910 μ l of PBS. DAPI was stained at last (1:1000) for 10 min. Single-color control samples were collected and stained for setting up the gating and compensation. Flow cytometry analyses were conducted using BD LSR II flow cytometer (BD Biosciences), and data were analyzed in FlowJo.

IF microscopy and IF quantification

IF microscopy was conducted using a Nikon A1R confocal microscope. Image processing and IF quantification were conducted on Fiji. For IF quantification, cell nuclei were stained with DAPI, and a viral marker was stained with the mouse IE1 primary antibody (clone 1B12; gift from T. Shenk) for HCMV infection, the ICP4 antibody (ab6514, Abcam) for HSV-1 infection, or the nucleoprotein (NP) antibody (gift from T. Shenk) for IAV infection. Alexa Fluor 633 rabbit anti-mouse IgG was used as the secondary antibody. Biological replicates represented different coculture wells, and one merged microscopic field was acquired for each well. Five-by-five merged images were taken using 20 \times objective lens, and three z-stacks were acquired with a 3- μ m step size. Eight-bit binning and max projection were applied to the images, and a median filter with 5- μ m pixel was set to remove speckles. Using the analyze particle function, the ratio of viral marker-positive particle number to DAPI-positive particle number is calculated as the proportion of superinfected cells in neighboring (GFP⁺/mCherry⁺) and distal (GFP⁻/mCherry⁻) populations. For each biological replicate, a minimum of 2000 cells were quantified (~3000 cells on average with a range of 2027 to 3799 cells). Approximately 160 primary infection events with 1:10 coculture ratio (range of 122 to 212 events) and ~500 primary infection events with a 1:3 coculture ratio (range of 335 to 676 events) were quantified. In the HCMV superinfection assay, we first determined the ratio (r) of IE1⁺ cells to VME primary infection events, representing IE1⁺ neighboring cells from the primary HCMV infection. Independently, we next superinfected an HCMV VME monolayer with an additional round of HCMV infection, exclusively quantifying neighboring cells that exhibited secondary HCMV infection by: $[(IE1^+) - r*(GFP^+)]/[(DAPI^+) - r*(GFP^+)]$.

Quantification and statistical analysis

Statistical analysis was performed using GraphPad Prism. Significance was determined by two-tailed Student's t test ($n = 3$ biological replicates) unless otherwise stated. Where applicable: * $P < 0.05$; ** $P < 0.01$; *** $P < 0.001$; **** $P < 0.0001$.

Supplementary Materials

This PDF file includes:

Figs. S1 to S6

Legends for tables S1 to S6

Other Supplementary Material for this manuscript includes the following:

Tables S1 to S6

[View/request a protocol for this paper from Bio-protocol.](#)

REFERENCES AND NOTES

- M. Carty, C. Guy, A. G. Bowie, Detection of viral infections by innate immunity. *Biochem. Pharmacol.* **183**, 114316 (2021).
- T. H. Mogensen, S. R. Paludan, Molecular pathways in virus-induced cytokine production. *Microbiol. Mol. Biol. Rev.* **65**, 131–150 (2001).
- K. D. Cook, S. N. Waggoner, J. K. Whitmire, NK cells and their ability to modulate T cells during virus infections. *Crit. Rev. Immunol.* **34**, 359–388 (2014).
- A. Lucas, G. McFadden, Secreted immunomodulatory viral proteins as novel biotherapeutics. *J. Immunol.* **173**, 4765–4774 (2004).
- J. Wang, F. Wu, C. Liu, W. Dai, Y. Teng, W. Su, W. Kong, F. Gao, L. Cai, A. Hou, C. Jiang, Exosomes released from rabies virus-infected cells may be involved in the infection process. *Virol. Sin.* **34**, 59–65 (2019).
- Y. Shi, L. Du, D. Lv, H. Li, J. Shang, J. Lu, L. Zhou, L. Bai, H. Tang, Exosomal interferon-induced transmembrane protein 2 transmitted to dendritic cells inhibits interferon alpha pathway activation and blocks anti-hepatitis B virus efficacy of exogenous interferon alpha. *Hepatology* **69**, 2396–2413 (2019).
- M. Kalamvoki, T. Du, B. Roizman, Cells infected with herpes simplex virus 1 export to uninfected cells exosomes containing STING, viral mRNAs, and microRNAs. *Proc. Natl. Acad. Sci. U.S.A.* **111**, E4991–E4996 (2014).
- S. Zicari, A. Arakelyan, R. A. N. Palomino, W. Fitzgerald, C. Vanpouille, A. Lebedeva, A. Schmitt, M. Bomsel, W. Britt, L. Margolis, Human cytomegalovirus-infected cells release extracellular vesicles that carry viral surface proteins. *Virology* **524**, 97–105 (2018).
- N. T. Streck, Y. Zhao, J. M. Sundstrom, N. J. Buchkovich, Human cytomegalovirus utilizes extracellular vesicles to enhance virus spread. *J. Virol.* **94**, e00609-20 (2020).
- D. L. Turner, D. V. Korneev, J. G. Purdy, A. de Marco, R. A. Mathias, The host exosome pathway underpins biogenesis of the human cytomegalovirus virion. *eLife* **9**, e58288 (2020).
- M. Suomalainen, U. F. Greber, Virus infection variability by single-cell profiling. *Viruses* **13**, 1568 (2021).
- M. Y. Hein, J. S. Weissman, Functional single-cell genomics of human cytomegalovirus infection. *Nat. Biotechnol.* **40**, 391–401 (2022).
- S. Jiang, C. N. Chan, X. Rovira-Clave, H. Chen, Y. Bai, B. Zhu, E. McCaffrey, N. F. Greenwald, C. Liu, G. L. Barlow, J. L. Weirather, J. P. Oliveria, T. Nakayama, I. T. Lee, M. S. Matter, A. E. Carlisle, D. Phillips, G. Vazquez, N. Mukherjee, K. Busman-Sahay, M. Nekorchuk, M. Terry, S. Younger, M. Bosse, J. Demeter, S. J. Rodig, A. Tzankov, Y. Goltsev, D. R. McLwain, M. Angelo, J. D. Estes, G. P. Nolan, Combined protein and nucleic acid imaging reveals virus-dependent B cell and macrophage immunosuppression of tissue microenvironments. *Immunity* **55**, 1118–1134.e8 (2022).
- L. Ombrato, E. Nolan, I. Kurelac, A. Mavousian, V. L. Bridgeman, I. Heinze, P. Chakravarty, S. Horswell, E. Gonzalez-Gualda, G. Maccachione, A. Weston, J. Kirkpatrick, E. Husain, V. Speirs, L. Collinson, A. Ori, J. H. Lee, I. Malanchi, Metastatic-niche labelling reveals parenchymal cells with stem features. *Nature* **572**, 603–608 (2019).
- F. Goodrum, The complex biology of human cytomegalovirus latency. *Adv. Virus Res.* **112**, 31–85 (2022).
- P. Griffiths, M. Reeves, Pathogenesis of human cytomegalovirus in the immunocompromised host. *Nat. Rev. Microbiol.* **19**, 759–773 (2021).
- C. S. Naucler, J. Geisler, K. Vetvik, The emerging role of human cytomegalovirus infection in human carcinogenesis: A review of current evidence and potential therapeutic implications. *Oncotarget* **10**, 4333–4347 (2019).
- S. Zeltzer, C. A. Zeltzer, S. Igarashi, J. Wilson, J. G. Donaldson, F. Goodrum, Virus control of trafficking from sorting endosomes. *MBio* **9**, e00683-18 (2018).
- K. C. Cook, E. Tsupurashvili, J. M. Needham, S. R. Thompson, I. M. Cristea, Restructured membrane contacts rewire organelles for human cytomegalovirus infection. *Nat. Commun.* **13**, 4720 (2022).
- I. Rodriguez-Sanchez, J. Munger, Meal for two: Human cytomegalovirus-induced activation of cellular metabolism. *Viruses* **11**, 273 (2019).
- B. S. Salvant, E. A. Fortunato, D. H. Spector, Cell cycle dysregulation by human cytomegalovirus: Influence of the cell cycle phase at the time of infection and effects on cyclin transcription. *J. Virol.* **72**, 3729–3741 (1998).
- J. E. Kim, Y. E. Kim, M. F. Stinski, J. H. Ahn, Y. J. Song, Human cytomegalovirus IE2 86 kDa protein induces STING degradation and inhibits cGAMP-mediated IFN- β induction. *Front. Microbiol.* **8**, 1854 (2017).
- K. Nightingale, M. Potts, L. M. Hunter, C. A. Fielding, C. M. Zerbe, A. Fletcher-Etherington, L. Nobre, E. C. Y. Wang, B. L. Strang, J. W. Houghton, R. Antrobus, N. M. Suarez, J. Nichols, A. J. Davison, R. J. Stanton, M. P. Weekes, Human cytomegalovirus protein RL1 degrades the antiviral factor SLFN11 via recruitment of the CRL4 E3 ubiquitin ligase complex. *Proc. Natl. Acad. Sci. U.S.A.* **119**, e2108173119 (2022).
- M. P. Weekes, P. Tomasec, E. L. Huttlin, C. A. Fielding, D. Nusinow, R. J. Stanton, E. C. Y. Wang, R. Aicheler, I. Murrell, G. W. G. Wilkinson, P. J. Lehner, S. P. Gygi, Quantitative temporal

- viromics: An approach to investigate host-pathogen interaction. *Cell* **157**, 1460–1472 (2014).
25. K. Nightingale, K. M. Lin, B. J. Ravenhill, C. Davies, L. Nobre, C. A. Fielding, E. Ruckova, A. Fletcher-Etherington, L. Soday, H. Nichols, D. Sugrue, E. C. Y. Wang, P. Moreno, Y. Umrana, E. L. Huttlin, R. Antrobus, A. J. Davison, G. W. G. Wilkinson, R. J. Stanton, P. Tomasec, M. P. Weekes, High-definition analysis of host protein stability during human cytomegalovirus infection reveals antiviral factors and viral evasion mechanisms. *Cell Host Microbe* **24**, 447–460.e11 (2018).
 26. D. Walsh, C. Perez, J. Notary, I. Mohr, Regulation of the translation initiation factor eIF4F by multiple mechanisms in human cytomegalovirus-infected cells. *J. Virol.* **79**, 8057–8064 (2005).
 27. D. M. Carter, K. Westdorp, K. R. Noon, S. S. Terhune, Proteomic identification of nuclear processes manipulated by cytomegalovirus early during infection. *Proteomics* **15**, 1995–2005 (2015).
 28. I. Moreno Jr., I. Rodriguez-Sanchez, X. Schafer, J. Munger, Human cytomegalovirus induces neuronal enolase to support virally mediated metabolic remodeling. *Proc. Natl. Acad. Sci. U.S.A.* **119**, e2205789119 (2022).
 29. R. T. Saffert, R. F. Kalejta, Inactivating a cellular intrinsic immune defense mediated by Daxx is the mechanism through which the human cytomegalovirus pp71 protein stimulates viral immediate-early gene expression. *J. Virol.* **80**, 3863–3871 (2006).
 30. R. J. Stanton, B. P. McSharry, C. R. Rickards, E. C. Wang, P. Tomasec, G. W. Wilkinson, Cytomegalovirus destruction of focal adhesions revealed in a high-throughput Western blot analysis of cellular protein expression. *J. Virol.* **81**, 7860–7872 (2007).
 31. T. Koshizuka, K. Tanaka, T. Suzutani, Degradation of host ubiquitin E3 ligase Itch by human cytomegalovirus UL42. *J. Gen. Virol.* **97**, 196–208 (2016).
 32. J. A. Fairley, J. Baillie, M. Bain, J. H. Sinclair, Human cytomegalovirus infection inhibits epidermal growth factor (EGF) signalling by targeting EGF receptors. *J. Gen. Virol.* **83**, 2803–2810 (2002).
 33. M. A. Kennedy, M. D. Tyl, C. N. Betsinger, J. D. Federspiel, X. Sheng, J. H. Arbuckle, T. M. Kristie, I. M. Cristea, A TRUSTED targeted mass spectrometry assay for pan-herpesvirus protein detection. *Cell Rep.* **39**, 110810 (2022).
 34. Y. Hashimoto, X. Sheng, L. A. Murray-Nerger, I. M. Cristea, Temporal dynamics of protein complex formation and dissociation during human cytomegalovirus infection. *Nat. Commun.* **11**, 806 (2020).
 35. J. L. Justice, M. A. Kennedy, J. E. Hutton, D. Liu, B. Song, B. Phelan, I. M. Cristea, Systematic profiling of protein complex dynamics reveals DNA-PK phosphorylation of IFI16 en route to herpesvirus immunity. *Sci. Adv.* **7**, eabg6680 (2021).
 36. W. A. Prinz, A. Toulmay, T. Balla, The functional universe of membrane contact sites. *Nat. Rev. Mol. Cell Biol.* **21**, 7–24 (2020).
 37. T. Shenk, J. C. Alwine, Human cytomegalovirus: Coordinating cellular stress, signaling, and metabolic pathways. *Annu. Rev. Virol.* **1**, 355–374 (2014).
 38. Z. Song, M. Ghochani, J. M. McCaffery, T. G. Frey, D. C. Chan, Mitofusins and OPA1 mediate sequential steps in mitochondrial membrane fusion. *Mol. Biol. Cell* **20**, 3525–3532 (2009).
 39. R. Hua, D. Cheng, E. Coyaud, S. Freeman, E. Di Pietro, Y. Wang, A. Vissa, C. M. Yip, G. D. Fairn, N. Braverman, J. H. Brumell, W. S. Trimble, B. Raught, P. K. Kim, VAPs and ACBD5 tether peroxisomes to the ER for peroxisome maintenance and lipid homeostasis. *J. Cell Biol.* **216**, 367–377 (2017).
 40. B. Reinhardt, M. Winkler, P. Schaarschmidt, R. Pretsch, S. Zhou, B. Vaida, A. Schmid-Kotsas, D. Michel, P. Walther, M. Bachem, T. Mertens, Human cytomegalovirus-induced reduction of extracellular matrix proteins in vascular smooth muscle cell cultures: A pathomechanism in vasculopathies? *J. Gen. Virol.* **87**, 2849–2858 (2006).
 41. I. Oelze, J. Kartenbeck, K. Crusius, A. Alonso, Human papillomavirus type 16 E5 protein affects cell-cell communication in an epithelial cell line. *J. Virol.* **69**, 4489–4494 (1995).
 42. Y. Ren, A. Wang, D. Wu, C. Wang, M. Huang, X. Xiong, L. Jin, W. Zhou, Y. Qiu, X. Zhou, Dual inhibition of innate immunity and apoptosis by human cytomegalovirus protein UL37x1 enables efficient virus replication. *Nat. Microbiol.* **7**, 1041–1053 (2022).
 43. S. R. Emmett, B. Dove, L. Mahoney, T. Wurm, J. A. Hiscox, The cell cycle and virus infection. *Methods Mol. Biol.* **296**, 197–218 (2005).
 44. Y. J. Song, M. F. Stinski, Inhibition of cell division by the human cytomegalovirus IE86 protein: role of the p53 pathway or cyclin-dependent kinase 1/cyclin B1. *J. Virol.* **79**, 2597–2603 (2005).
 45. N. Caffarelli, A. R. Fehr, D. Yu, Cyclin A degradation by primate cytomegalovirus protein pUL21a counters its innate restriction of virus replication. *PLOS Pathog.* **9**, e1003825 (2013).
 46. M. Zydek, C. Hagemeyer, L. Wiebusch, Cyclin-dependent kinase activity controls the onset of the HCMV lytic cycle. *PLOS Pathog.* **6**, e1001096 (2010).
 47. J. P. Alao, The regulation of cyclin D1 degradation: Roles in cancer development and the potential for therapeutic intervention. *Mol. Cancer* **6**, 24 (2007).
 48. J. L. Justice, I. M. Cristea, Nuclear antiviral innate responses at the intersection of DNA sensing and DNA repair. *Trends Microbiol.* **30**, 1056–1071 (2022).
 49. R. F. Kalejta, J. T. Bechtel, T. Shenk, Human cytomegalovirus pp71 stimulates cell cycle progression by inducing the proteasome-dependent degradation of the retinoblastoma family of tumor suppressors. *Mol. Cell Biol.* **23**, 1885–1895 (2003).
 50. M. N. Prichard, Function of human cytomegalovirus UL97 kinase in viral infection and its inhibition by maribavir. *Rev. Med. Virol.* **19**, 215–229 (2009).
 51. L. A. Murray-Nerger, J. L. Justice, P. Rekapalli, J. E. Hutton, I. M. Cristea, Lamin B1 acetylation slows the G1 to S cell cycle transition through inhibition of DNA repair. *Nucleic Acids Res.* **49**, 2044–2064 (2021).
 52. P. Strzyz, BCL-2 proteins feed their own expression. *Nat. Rev. Mol. Cell Biol.* **18**, 652–653 (2017).
 53. M. S. Crow, K. K. Lum, X. Sheng, B. Song, I. M. Cristea, Diverse mechanisms evolved by DNA viruses to inhibit early host defenses. *Crit. Rev. Biochem. Mol. Biol.* **51**, 452–481 (2016).
 54. E. Rognoni, A. O. Pisco, T. Hiratsuka, K. H. Sipila, J. M. Belmonte, S. A. Mobasser, C. Philippeos, R. Dilao, F. M. Watt, Fibroblast state switching orchestrates dermal maturation and wound healing. *Mol. Syst. Biol.* **14**, e8174 (2018).
 55. K. Suzuki, K. Takahashi, Reduced cell adhesion during mitosis by threonine phosphorylation of beta1 integrin. *J. Cell. Physiol.* **197**, 297–305 (2003).
 56. B. Bogdanow, Q. V. Phan, L. Wiebusch, Emerging mechanisms of G1/S cell cycle control by human and mouse cytomegaloviruses. *MBio* **12**, e0293421 (2021).
 57. M. S. Schrock, B. R. Stromberg, L. Scarberry, M. K. Summers, APC/C ubiquitin ligase: Functions and mechanisms in tumorigenesis. *Semin. Cancer Biol.* **67**, 80–91 (2020).
 58. M. Eifler, R. Uecker, H. Weisbach, B. Bogdanow, E. Richter, L. Konig, B. Vetter, T. Lenac-Rovis, S. Jonjic, H. Neitzel, C. Hagemeyer, L. Wiebusch, PUL21a-cyclin A2 interaction is required to protect human cytomegalovirus-infected cells from the deleterious consequences of mitotic entry. *PLOS Pathog.* **10**, e1004514 (2014).
 59. T. Bodrug, K. A. Welsh, M. Hinkle, M. J. Emanuele, N. G. Brown, Intricate regulatory mechanisms of the anaphase-promoting complex/cyclosome and its role in chromatin regulation. *Front. Cell Dev. Biol.* **9**, 687515 (2021).
 60. L. Hertel, S. Chou, E. S. Mocarski, Viral and cell cycle-regulated kinases in cytomegalovirus-induced pseudomitosis and replication. *PLOS Pathog.* **3**, e6 (2007).

Acknowledgments: We thank G. Laevsky and S. Wang from Princeton University Microscopy Facility as well as C. J. DeCoste and K. Rittenbach from Princeton University Flow Cytometry Resource Facility for technical support. We thank J. E. Hutton for maintenance of MS instruments and technical support. **Funding:** We are grateful for funding provided by NIH NIGMS (GM114141), NIH NIAID (AI174515), and Stand Up To Cancer Convergence 3.1416 to I.M.C.; China Scholarship Council (CSC) scholarship (201506210052) to B.S.; NIH NCATS TL1 award (TL1TR003019) to K.K.L.; NIH NIAID Predoctoral Fellowship (F31AI147637) to K.C.C.; and the NIH Training Grant from NIGMS (T32GM007388). **Author contributions:** X.S., B.S., and I.M.C. conceptualized the study. B.S., X.S., J.L.J., K.K.L., P.J.M., K.C.C., J.C.K., and I.M.C. contributed to the investigation and methodology. Data curation, analysis, visualization, and validation were carried out by B.S., X.S., J.L.J., K.K.L., and I.M.C. **Competing interests:** The authors declare that they have no competing interests. **Data and materials availability:** All data needed to evaluate the conclusions in the paper are present in the paper and/or the Supplementary Materials. The MS data for VME proteomes have been deposited to the ProteomeXchange Consortium via the PRIDE partner repository with the dataset identifier PXD038547 and PXD040582. MCS and viral protein PRM MS data have been deposited to Panorama Public (<https://panoramaweb.org/vm-memcsprm.url>), associated with the ProteomeXchange ID PXD038466.

Submitted 19 December 2022

Accepted 7 April 2023

Published 10 May 2023

10.1126/sciadv.adg3433